Computational Characterization of Thermal Processes in an AlN:Mo Susceptor in a Millimeter Wave Heat Exchanger

by

Stephanie Martin

A Thesis

Submitted to the Faculty

of the

WORCESTER POLYTECHNIC INSTITUTE

in partial fulfillment of the requirements for the

Degree of Master of Science

in

Industrial Mathematics

by

April 2019

Approved by:

Dr. Vadim V. Yakovlev, Thesis Advisor

Dr. Luca Capogna, Department Head

Abstract

Electromagnetic (EM) heating is applied in a wide range of areas such as food engineering, chemistry, and materials science. Recent developments suggest using this technology in EM heat exchangers for solar energy collectors, microwave thermal thrusters, and ground-to-ground millimeter-wave (MMW) power beaming. These devices convert EM energy into usable thermal energy, relying on the balanced interactions between EM, heat transfer, and fluid flow phenomena. This means the interactions between the MMW field and an absorbing ceramic element of a heat exchanger need to be well understood to develop an efficient device in which the material is controllably heated and the heat is efficiently transferred to another medium (e.g. fluid).

In this work, we develop a computational model to simulate EM and thermal processes in a simplified MMW heat exchanger and examine different ceramic materials to find the one that maximizes the device's efficiency. EM and EM-thermal coupled problems are solved by the finite-difference time-domain (FDTD) technique (implemented in *QuickWave*) for a block of AlN:Mo composite that is backed by a thin metal plate and irradiated by a MMW plane wave. Computation is based on experimental data on temperature-dependent dielectric constant, loss factor, specific heat, and thermal conductivity. In addition to the case of full thermal insulation of the ceramic block (Neumann scenario), with a Dirichlet boundary condition on the surface between the metal plate and the ceramic block, we imitate a special operational regime in which the metal plate is maintained at a constant temperature to prevent the ceramic block from overheating.

The FDTD model is verified by solving the underlying EM problem by the finite-element simulator, *COMSOLMultiphysics*. It is shown that in the considered scenario with the Dirichlet boundary condition, accuracy of the iterative FDTD solution of the coupled EM-thermal problem strongly depends on the heating time step: maintaining a high temperature on the interface with the metal plate triggers higher levels of non-uniformity of temperature fields and requires a smaller time step to achieve a sufficient level of adequacy. It is shown that, at 95 GHz, 10x10x10 mm blocks with Mo contents from 0.25 to 4% can be heated up to 1,000 C highly uniformly for 60-95s, depending on the percentage of Mo. The composite producing the highest level of total dissipated power in both the Neumann and Dirichlet scenarios is found to have Mo concentration around 3%; this composite is recommended for use in the first physical prototype of a MMW heat exchanger.

Acknowledgements

I would first like to thank my thesis advisor Professor Vadim Yakovlev of the Mathematical Science Department for his continuous support and guidance throughout the year. I would also like to thank Dr. Brad W. Hoff, AFRL, Kirtland AFB and Dr. Ian M. Rittersdorf, NRL, for their permanent interest, constructive comments and crucial suggestions.

I would like to thank my fellow students, Ajit A. Mohekar, Ph.D. student, Mechanical Engineering Department, for providing help with modeling in COMSOL Multiphysics, and Petra Kumi ('20), undergraduate student, Departments of Mathematical Sciences and Computer Science Department, for her guidance in post-processing the output data from *QuickWave* using MATLAB. I would also like to thank Dr. Marzena Olszewska-Placha, QWED, for her instructive technical support in handling challenging issues in *QuickWave*, as well as the Department of Academic Research Computing, WPI, for providing access to required software (COMSOL) and hardware needed for this work.

The material of this Thesis is based on research supported by the Air Force Research Laboratory, Leidos, Inc./ARFL, Grant No P010200226.

Contents

1 Introduction **1**

2 Applicable Numerical Techniques **5**

2.1 Related principles of Finite Element Method 5

2.1.1 The Galerkin Method 5

2.1.2 Boundary Conditions 6

2.2 Related principles of Finite Difference Method 7

2.3 Finite-Difference Time-Domain Technique and a Coupled EM-Thermal Problem . . 9

3 Material Properties of a Ceramic Susceptor **11**

3.1 Applicable Ceramic Materials 11

3.2 AlN:Mo Composite: Experimental Data on Electromagnetic Parameters 13

3.3 AlN:Mo Composite: Experimental Data on Thermal Parameters 17

4 Computational Model **18**

4.1 The FDTD Model 18

4.2 Input Data for the EM-Thermal Model 21

4.3 Thermal Boundary Conditions 22

4.4 Benchmarking of the FDTD Model Against a COMSOL Model 23

4.5 Post-Processing Data of Dissipated Power with MATLAB 24

5 Thermal Processes under Full Thermal Insulation of the AlN:Mo Susceptor **26**

5.1 Ceramic Block without a Metal Plate 26

5.2 Patterns for Dissipated Power Density 28

5.3 Time Evolution of Temperature Fields 30

5.4 Results for Total Dissipated Power 32

6 Thermal Processes under the Condition of Constant Temperature on the Back Surface 35

6.1 Effect of Heating Time Step in the FDTD Model 36

6.2 Time Evolution of Temperature Fields 39

6.3 Total Dissipated Power 40

7 Conclusion 41

7.1 Computer Model 41

7.2 Operational Functionality of the Susceptor 42

7.3 Future Computational Studies 42

Appendices 44

A MATLAB Procedure 45

B *.pmo Files 48

C *.pm2 Files 51

List of Figures

1.1 Concept of a MMW HX. 2

2.1 The FDTD algorithm for solving a coupled EM-thermal problem [20, 21]. 10

3.1 Thermal conductivity for applicable ceramic materials [27]. 12
3.2 Data on measurement of dielectric constants for each concentration of Mo. 13
3.3 Data on measurement of loss factors for each concentration of Mo. 14
3.4 Polynomial approximations for new specific heat capacity values based on experimental data. 15
3.5 Polynomial approximations for new thermal conductivity values based on experimental data. 16

4.1 Rectangular AlN:Mo susceptor with a metal plate attached to the back surface - the scenario reproduced in the model. 19
4.2 EM boundary conditions in the model. 19
4.3 FDTD mesh in the model. 20
4.4 Input data for the FDTD coupled EM-thermal model in *QuickWave* for 3.0% Mo. . 22
4.5 Comparison of patterns of density of dissipated power: the FEM (*COMSOL Multiphysics*) and FDTD (*QuickWave*) models. 24
4.6 Diagram of the visualization procedure for MATLAB. 24
4.7 Examples of 2D and 3D MATLAB visualizations of dissipated power in a particular plane of the ceramic block. 25

5.1 Patterns of density of dissipated power in the absence of the metal plate and full thermal insulation of the AlN:Mo block at $T = 20$°C; maximum value of P_d is shown under each pattern; power of incoming plane wave $P = 100$W. 27

5.2 True characteristics of minimum and maximum temperatures in the AlN:Mo block; no metal plate; $P = 30$ and 100W. 27
5.3 Total power absorbed at different temperatures of the AlN:Mo block; no metal plate; $P = 100$W. 28
5.4 Patterns of dissipated power density in the presence of the metal plate on the back surface and with full thermal insulation of the AlN:Mo block with Mo = 0.25, 1.0, and 3.0% for the block's temperature of 20°C (a) and 800°C (b); $P = 100$ W. 29
5.5 Temperature distributions on the back surface (YZ-plane) of the AlN:Mo block with Mo = 0.25, 0.5, 1.0, 2.0, 3.0, and 4.0% along with maximum values of temperature (T_{max}) in each pattern. Patterns are normalized to the minimum temperature of the process (20°C); heating time steps are 5 (Mo = 0.25 and 0.5%), 2.5 (Mo = 1.0 and 2.0%), and 2.0 s (Mo = 3.0 and 4.0%); $P = 100$ W; $t = 10$ mm. 31
5.6 Time characteristics of minimum and maximum temperatures in the AlN:Mo block; full thermal insulation; $P = 30$ and 100W. 32
5.7 Total power absorbed at different temperatures of the AlN:Mo block; thin metal plate on back surface; $P = 100$W. 33
5.8 Energy efficiency of the block with and without a metal plate. 33

6.1 Maximum temperature in the block for different heating time steps with metal plate held at constant 700 C for 0.25% Mo and $P = 100$W (a); error for heating time steps with respect to 0.01s for all concentrations (b); Mo = 0.25%, $T_c = 700$°C, $P = 100$W. 36
6.2 Maximum temperature in the block for different heating time steps with full thermal insulation for both 0.25% and 1.0% Mo at $P = 100$W. 37
6.3 Normalized temperature patterns in the block in the central XY-plane with metal plate held at constant 700 C for Mo = 0.25% (a) and Mo = 3.0% (b) with $P = 100$W. 38
6.4 Maximum temperature in the block for different concentrations of Mo with metal plate held at constant 600, 700, and 800 C for $P = 100$W. 38
6.5 Maximum temperature in the block with $P = 100$W and metal plate held at constant (a) 600 C (b) 700 C and (c) 800 C for all concentrations of Mo. 39
6.6 Absorbed power in the block when the plate is held at $T_c = 600$, 700, and 800°C with $P = 100$W. 40

List of Tables

3.1 Polynomial Approximations for the Dielectric Constant Values. 13

3.2 Polynomial Approximations for the Loss Factor Values. 14

3.3 Density of the Ceramic Materials. 14

3.4 Polynomial approximations for the updated specific heat capacity values. 15

3.5 Polynomial approximations for the updated thermal conductivity values. 16

4.1 Dielectric Properties of the Ceramic Materials at 20 and 1000 C at $f = 95$ GHz. . . 21

4.2 Sizes of FDTD Cells (in mm) in the Model Operating at $f = 95$ GHz. 21

4.3 Parameters of the Test Scenario for Benchmarking of the FDTD Model. 23

Chapter 1

Introduction

Electromagnetic (EM) heating is commonly employed in a variety of areas including food engineering, chemistry, and materials science [1]–[5]. More recently the technology has been used in microwave thermal thrusters [6][7] and EM heat exchangers (HX) for ground-to-ground millimeter-wave (MMW) power beaming applications [8]–[11]. The latter devices convert EM energy into useful mechanical work, with their functionality strongly depending on the combined effects of EM, heat transfer, and fluid flow phenomena. This means that interactions of the MMW field with a ceramic element of a HX should be well understood for effectively utilizing EM energy, controllably heating the material, and transferring heat to another medium, such as a fluid. This makes multi-physics modeling capable of adequately simulating all essential physical effects a favorable design tool for an efficient MMW HX.

A new type of MMW-powered HX currently under development consists of an assembly of ceramic tiles arranged in a rectangle with small air gaps between each to allow for expansion during heating. The back surface of the tiles is attached to a metal baseplate containing channels with fluid flow, as pictured in Figure 1.1. Due to dielectric losses, EM power is dissipated in the absorbing tiles, and the induced thermal field heats the attached baseplate. This in turn heats the fluid flowing in the channels. In an efficient device, the ceramic material used in the tiles should possess special EM and thermal properties, such as high loss factor, high thermal conductivity, an ability to withstand high temperatures (up to 1000-1500°C) and high thermal

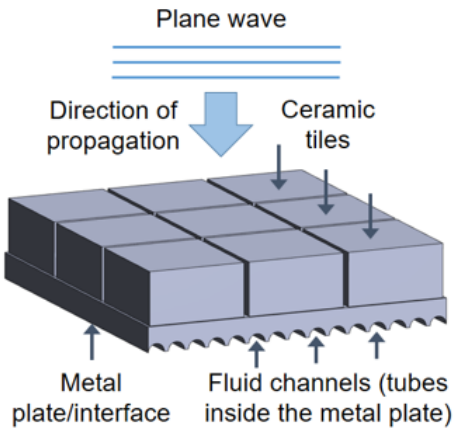

Figure 1.1: Concept of a MMW HX.

gradients. While a particular material can appear generally attractive from some initial experiments, determining the device's practical dimensions and optimal material properties needed to ensure energy efficient operations in the desired temperature regime would require particularly extensive experimentation. Moreover, distribution of the heat on the ceramic-metal interface is very important, but measuring temperature patterns there is a challenging task. How heat transfers from the metal plate to the fluid depends on the material parameters, speed, and other characteristics of the latter and is also difficult to predict. Thus comprehensive modeling exploring the EM, thermal, and fluid dynamics phenomena in an appropriate model of a MMW HX is highly desired. The recent reports [12][13] directly address this need, but these studies are focused on the mathematical characterization of the related physical processes in idealized three-layer structures and are not sufficiently instructive for this system's design.

In order to fully model a MMW HX, one must solve three problems - one in electromagnetics, one in heat transfer, and one in fluid dynamics. Because of the enormous complexity of a comprehensive model for all three physics, it is feasible to build it in stages. Following the sequence of phenomena, the first model is the EM one, which computes both the EM fields and dissipated power. The second model couples the EM and heat transfer processes to investigate temperature fields. The third model would then add fluid dynamics to include parameters of the fluid. This approach should provide the opportunity to make sure the that first model is adequate and sufficiently accurate before moving on to the next and help simplify a complex series of problems.

The Finite Element Method (FEM) and the Finite Difference Method (FDM) are two numerical techniques that could be applicable to the three physics in the outlined approach. The FEM dis-

cretizes a domain into a finite number of elements, derives governing equations for those elements, and then solves them using matrix operations. The FDM approximates a continuous domain with a mesh of discrete points, replacing derivatives with finite difference equations. The FEM was adapted to electromagnetics in the 1970s and has been used successfully in the field, but it requires a very large number of equations, demanding extensive computational resources and making prediction of computational time difficult. The Finite-Difference Time-Domain (FDTD) method was introduced specifically for solving high-frequency EM problems, approximating both the space and time derivatives of Maxwell's equations with the central-difference formula. Computing time for the FDTD method is predictable and the technique is computationally less extensive compared to the FEM, as it does not require handling huge matrices [14][15]. When solving electrically large problems at high frequencies, FDTD appears to be more efficient and requires significantly less computer memory/resources than the FEM [14][16], making it the more advantageous technique for modelling the EM problem of a MMW HX. On the other hand, the FEM is a standard, powerful option for solving thermal and fluid dynamics problems.

At the moment, no computational algorithm reported in literature can be applied directly to all physics in the device in question. Several publications address related problems, but their techniques are not applicable to this specific one. For instance, in [17], the authors use the FDTD method with the heat transport equation to get wave absorption characteristics of an absorber irradiated by an EM field, but the problem is set up in a waveguide. In [18], the authors develop a coupled EM and thermal ODE model for microwave heating, but demonstrate its functionality for only the 1D case, providing no evidence of practicality of the use of their model in real-life scenarios.

In this Thesis, we address the need in CAD tools for MMW HX by starting the development of suitable EM and EM-thermal models. We study the process of heating a rectangular block of an aluminum nitride-molybdenum composite (AlN:Mo) by a normally incident plane MMW through EM and coupled EM-thermal modeling using the FDTD method. The block is backed by a thin metal plate. Six material compositions are considered by analyzing samples with different Mo concentration (by volume), ranging from 0.25 to 4.0% Mo. Experimental data on temperature-dependent characteristics of EM (at 95 GHz) and thermal material parameters are approximated and extrapolated to be used as input data for the coupled EM-thermal simulation. In the framework of EM modeling, heating of the ceramic samples is characterized by volumetric patterns of density of dissipated power for the dielectric constant and loss factor corresponding to different temperatures

of the process. EM-thermal coupled modeling is run in the range from 20 to 1,000°C as an iterative procedure in which EM and thermal material parameters are upgraded in every cell after each heating time step; the process in this case is represented by a series of temperature patterns showing time evolution of the thermal field.

Additionally, we benchmark the EM portion of the FDTD model by solving the problem with the finite element method. A direct benchmarking is not possible because of the excessive computational resources required by the FEM algorithm. Thus, the comparison is done at a lower frequency (2.45 GHz) with zirconia, whose EM and thermal material parameters at 2.45 GHz are known (in contrast to AlN:Mo).

Two thermal boundary condition cases for the coupled FDTD model are considered in this work. In the first case, all faces of the ceramic block have Neumann boundary conditions, imitating full thermal insulation. In terms of homogeneity, the temperature fields are shown to be exceptionally uniform for all concentrations of Mo and throughout the entire temperature range. We contribute this effect to high thermal conductivity of the AlN:Mo composite. In the second case, a Dirichlet boundary condition is applied on the surface between the ceramic block and the metal plate, with all other faces remaining thermally insulated. The metal plate is held at some high constant temperature, from 600 to 800°C, to prevent the ceramic block from overheating. It is shown that after 15-20s, the temperature profiles in the AlN:Mo samples achieve equilibrium and the thermal gradients do not exceed 60-90°C. The effect of heating time step on the accuracy of results in this scenario is also observed, where as it does not happen in the first scenario. In terms of the level of absorbed power, the composite with Mo ~3% appears to provide the highest energy efficiency in both cases and, as such, is recommended for the use in a physical prototype.

While the first case is not practical in real-life applications, it is needed to see the temperature distributions in the AlN:Mo block as functions of relevant parameters. The second case mimics an operational regime of the MMW HX; however, the block remains thermally insulated on all but one side, which may not be held in real-life applications. Thus, we acknowledge that further study involving alternative thermal boundary conditions is needed to fully model the problem at hand.

Chapter 2

Applicable Numerical Techniques

The Finite Element Method and the Finite Difference Method are the two most practical numerical techniques in terms of accuracy, capability, and resources when it comes to solving a coupled EM-thermal problem. This section provides a brief overview of basic principles of both methods along with their pros and cons. The review follows the consideration of the methods in [19] and is based on the differential equations characterizing 1D heat transfer problems.

2.1 Related principles of Finite Element Method

The Finite Element Method (FEM) is based on integral minimization of error and, in general, can handle more complex geometries than FDM. There are three basic steps in the FEM:

1. It divides the region into many elements.
2. A solution to the differential equation is approximated for each element through interpolation polynomials.
3. When considered together, all the elements create the finite representation of the region.

2.1.1 The Galerkin Method

The one dimensional heat conduction equation at steady state is

$$k\frac{d^2T}{dx^2} + \dot{q} = 0.$$

where k is the thermal conductivity, T is temperature, and q is the quantity of heat. The first step in the finite element method is to divide the region of interest into n elements. Then the temperature distribution can be estimated by

$$T(x) = T_1\phi_1(x) + T_2\phi_2(x) + ... + T_{n+1}\phi_{n+1}(x) = \sum_{i=1}^{n+1} T_i\phi_i,$$

where $\phi_i(x)$ are functions that describe the shape of the region and T_i are temperature constants. Since this gives an approximation to the solution, there is an error, known as the residue, which is represented as

$$R = k\frac{d^2T}{dx^2} + \dot{q}.$$

The Galerkin method uses weighted residuals to minimize the residue by making it vanish at each node in the mesh. The shape functions are used as the weighting functions $w_i(x)$ in the Galerkin method and are multiplied by the residue $R(x)$. The integral from $x = 0$ to $x = L$ (the length of the region) of this product is set to zero to make the residue vanish:

$$\begin{aligned}
&\int_0^L w(x)R(x)dx \\
&= \int_0^L \phi(x)\Big[-k\frac{d^2T}{dx^2} - \dot{q}\Big]dx \\
&= \int_0^L k\frac{dT}{dx}\frac{d\phi}{dx} - k\phi\frac{dT}{dx}\Big|_0^L - \int_0^L \phi(x)\dot{q}]dx = 0.
\end{aligned}$$

2.1.2 Boundary Conditions

With Dirichlet boundary conditions, the shape function at the boundary is set to zero. For example, if $T(x = 0)$ is given, $\phi(0) = 0$:

$$-k\phi\frac{dT}{dx}\Big|_{x=0} = 0$$

With Neumann or Mixed boundary conditions, the term $-k\phi\frac{dT}{dx}\Big|_0^L$ in the Galerkin method equation is replaced with the corresponding heat flux and shape function. For a known heat flux at $x = L$:

$$\begin{aligned}
-k\frac{dT}{dx}\Big|_{x=L} &= q'', \\
-k\phi\frac{dT}{dx}\Big|_{x=L} &= \phi(L)q'',
\end{aligned}$$

and for a convection condition at $x = L$:

$$-k\frac{dT}{dx}\Big|_{x=L} = \phi(L)h(T - T_\infty).$$

where h is the convection heat transfer coefficient. However, the shape function is usually set to 1 ($\phi(L) = 1$). As noted in the derivation,

$$T(x) = \sum_{i=1}^{n+1} T_i\phi_i(x),$$

giving the final equation:

$$\sum_{i=1}^{n+1} T_i\Big[\int_0^L k\frac{d\phi_j}{dx}\frac{d\phi_i}{dx}\Big] - k\phi_i\frac{dT}{dx}\Big|_{x=0} - \int_0^L \phi_i\dot{q}dx = 0.$$

Therefore, the FEM approximates a differential equation through interpolation polynomials for each element in the mesh, then solves them using matrix operations. The FEM can be used to approximate higher-dimensional heat equations, as well as other physics equations, which can be practical in solving the mutiphysics problem in this study.

2.2 Related principles of Finite Difference Method

The Finite Difference Method (FDM) approximates a continuous domain with a mesh of discrete points. The key step of the method is that, based on the Taylor series expansion, it replaces the partial derivatives and boundary conditions with finite difference approximations.

An equation formulated in terms of partial derivatives is required to apply the finite difference method to the heat conduction equation. Let $f = f(x, y)$ and hold y constant. Then the finite difference approximation for $\frac{\partial f}{\partial x}$ can be derived as follows.

The function f can be expanded with a Taylor series as:

$$f(x + \Delta x, y) = f(x, y) + \frac{\partial f}{\partial x}(x, y)\Delta x + \frac{\partial^2 f}{\partial x^2}(x, y)\frac{\Delta x^2}{2} + \frac{\partial^3 f}{\partial x^3}(x, y)\frac{\Delta x^3}{6} + O(\Delta x^4)$$

and

$$f(x - \Delta x, y) = f(x, y) - \frac{\partial f}{\partial x}(x, y)\Delta x + \frac{\partial^2 f}{\partial x^2}(x, y)\frac{\Delta x^2}{2} - \frac{\partial^3 f}{\partial x^3}(x, y)\frac{\Delta x^3}{6} + O(\Delta x^4).$$

This yields the forward difference equation

$$\frac{\partial f}{\partial x}(x,y) = \frac{f(x+\Delta x,y) + f(x,y)}{\Delta x} + O(\Delta x)$$

and backward difference equation

$$\frac{\partial f}{\partial x}(x,y) = \frac{f(x,y) - f(x-\Delta x,y)}{\Delta x} + O(\Delta x)$$

respectively. Subtracting the two yields the central difference equation

$$\frac{\partial f}{\partial x}(x,y) = \frac{f(x+\Delta x,y) - f(x-\Delta x,y)}{2\Delta x} + O(\Delta x^2),$$

while adding them together results in the approximation for the second derivative with respect to x

$$\frac{\partial^2 f}{\partial x^2}(x,y) = \frac{f(x+\Delta x,y) - 2f(x,y) + f(x-\Delta x,y)}{(\Delta x)^2} + O(\Delta x)^2.$$

All of the above expressions can also be translated for $f(x, y+\Delta y)$.

The FDM can then be applied to the transient heat conduction equation in one dimension:

$$\frac{\partial T}{\partial t} = \alpha \frac{\partial^2 T}{\partial x^2},$$

where

$$\alpha = \frac{k}{\rho C_\rho}$$

is the thermal diffusivity, k is the thermal conductivity, ρ is the density, and C_ρ is the heat capacity; These parameters are assumed to be constant, and it is assumed that there are no heat generating sources.

The rate of temperature change $\frac{\partial T}{\partial t}$ can be approximated with the forward finite difference method:

$$\frac{\partial T}{\partial t} = \frac{T_i^{n+1} - T_i^n}{\Delta t},$$

and the spatial derivative $\frac{\partial^2 T}{\partial x^2}$ can be approximated with the central difference formula:

$$\frac{\partial^2 T}{\partial x^2} = \frac{T_{i+1}^n - 2T_i^n + T_{i-1}^n}{(\Delta x)^2}.$$

Substituting these equations into the heat conduction equation gives

$$\frac{T_i^{n+1} - T_i^n}{\Delta t} = \alpha(\frac{T_{i+1}^n - 2T_i^n + T_{i-1}^n}{(\Delta x)^2}),$$

and rearranging the terms gives the final explicit scheme:

$$T_i^{n+1} = T_i^n + \alpha\Delta t(\frac{T_{i+1}^n - 2T_i^n + T_{i-1}^n}{(\Delta x)^2}).$$

Applying initial and boundary conditions and iterating until a set threshold is met will result in an approximation of the temperature distribution at time t.

To summarize, the FDM approximates differential equations with finite difference approximations, taking a continuous domain and dividing it into discrete points. The FDM can be applied to higher-dimensional heat equations as well as other physics equations, making it a useful candidate for this study.

The Finite Difference and Finite Element methods both have strengths and weaknesses and which one to use depends on the project and available computing power. In general, for modeling electrically large scenarios (i.e., ones in which the dimensions of the object are comparable to the wavelength in the medium), the FDM may require modest resources to calculate a solution, whereas the FEM may be computationally intensive. On the other hand, if the goal of the modeling project is to provide direct assistance in system design rather than to develop a mathematical characterization of the related idealized scenario, the modeler would need to use advanced commercially available simulators instead of attempting to build the model from the underlying differential equations, e.g., the ones in Sections 2.1 and 2.2.

2.3 Finite-Difference Time-Domain Technique and a Coupled EM-Thermal Problem

In general, the EM and heat transfer problems addressed in this study are coupled as follows. The heat transfer in a media is given by:

$$(\rho C_\rho)\frac{\partial T}{\partial t} + \rho C_\rho \nabla T = \nabla(k\nabla T) + Q_{gen}$$

where Q_{gen} is the heat source associated with the power absorbed from the wave

$$Q_{gen} = \sigma_e E^2 = 2\pi f \epsilon_0 \epsilon'' E^2$$

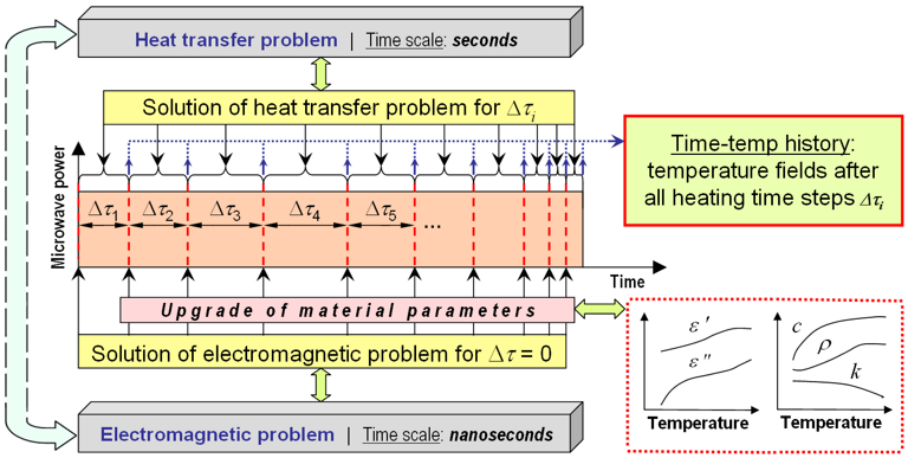

Figure 2.1: The FDTD algorithm for solving a coupled EM-thermal problem [20, 21].

where σ_e is the electrical conductivity, f is the frequency, and E is the electric field.

Overall, in the context of the three physics involved in the operation of a MMW HX, i.e., electromagnetics, heat transfer, and fluid dynamics, the options are clearly reduced to the choice of an adequate multiphysics simulator. In accordance with the reviews of available computational tools applicable to EM heating problems [16][20][21], for modeling of EM and EM-thermal processes (which the present study is dedicated to), the feasible choice is the 3D conformal FDTD simulator $QuickWave^{\text{TM}}$ coupled with the special thermal unit $QW\text{-}BHM^{\text{TM}}$ in the $QuickWave$ package [22].

In the $QuickWav$ environment, there is an option for the full-wave numerical solution of two-way coupled EM and thermal problems emerging in scenarios associated with microwave and MMW heating. The procedure to be employed for coupling the two solvers may be similar to the ones outlined in [15][20][23][24]. The algorithm outlined in Figure 2.1 starts by solving the EM problem as if it occurs instantaneously due to its very small time scale (nanoseconds); the EM solution is then used to solve the heat transfer problem in real time (seconds). The solvers operate as parts of an iterative procedure in which a steady state solution of the EM problem becomes an input for the thermal problem, and, in the repeated runs of the EM solver, material parameters are upgraded in every cell in accordance with the temperature field outputted from the thermal solver. The latter determines temperature distribution induced after each heating time step Δt; N steps are needed to reach the maximum temperature of the process. The cycle continues for a specified heating time.

Chapter 3

Material Properties of a Ceramic Susceptor

3.1 Applicable Ceramic Materials

The operational functionality of a MMW HX requires the use, as a susceptor, of a ceramic material characterized by both high dielectric losses (to absorb much of the power of the incoming EM wave) and high thermal conductivity (to effectively spread the generated heat through the susceptor's volume and transfer it to the metal baseplate). The ceramic susceptor must also have the ability to withstand high temperatures and a significant thermal gradient in relatively small volumes. Other important factors include low cost, commercial availability, and manufacturing capabilities for mass production.

In the development of the MMW HX in the AFRL at Kirtland AFB, all these criteria were accounted for when choosing the most suitable ceramic material for the susceptor. Thermal conductivity was taken as the leading criterion in choosing the ceramic matrix for the susceptor [25][26]. Multiple ceramic materials were considered, including Beryllium Oxide, Aluminum Nitride, Silicon Carbide, Boron Nitride, and Aluminum Oxide, which all have high thermal conductivity, as shown in Figure 3.1. Beryllium Oxide has the highest thermal conductivity, but due to its hazardous nature it is not a feasible choice. The material with the next highest thermal conductivity is Aluminum Nitride (AlN), which is the material chosen in the present development.

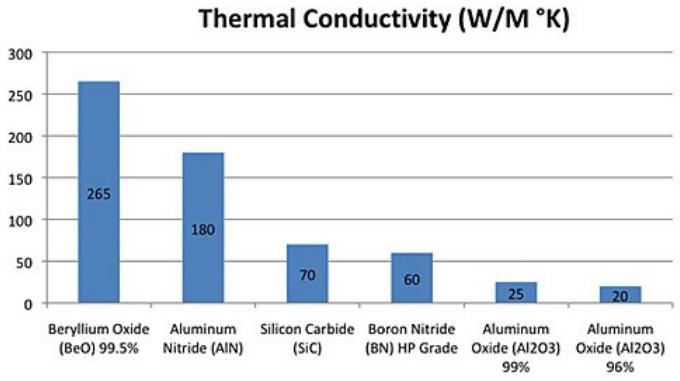

Figure 3.1: Thermal conductivity for applicable ceramic materials [27].

In terms of the loss factor, it was also suggested that the effective dielectric losses of the susceptor composite should be dominated by contributions from the additive material [26]. EM and thermal material parameters of ceramic materials are known to be temperature-dependent and, as such, they condition particular behavior of the related devices at high temperatures [24][28]–[30]. In this context, the temperature-dependent loss factor should be as weakly exponential as possible in order to limit the likelihood of thermal runaway [31] and to better enable optimal material performance over a wide range of operating temperatures.

One such type of ceramic composite currently under investigation for the use in a MMW susceptor is AlN containing metallic Mo powder (AlN:Mo). In order to model a MMW HX based on this composite and characterize its suitability for the susceptor material, the EM and thermal properties of the material were determined for a wide range of temperatures and six concentration of Mo: 0.25, 0.5, 1.0, 2.0, 3.0, and 4.0% (by volume).

In the following sections of this Chapter, we present experimental data for the EM and thermal material parameters of a series of AlN:Mo samples and the processing of this data for converting it into the input data for the EM-thermal coupled model.

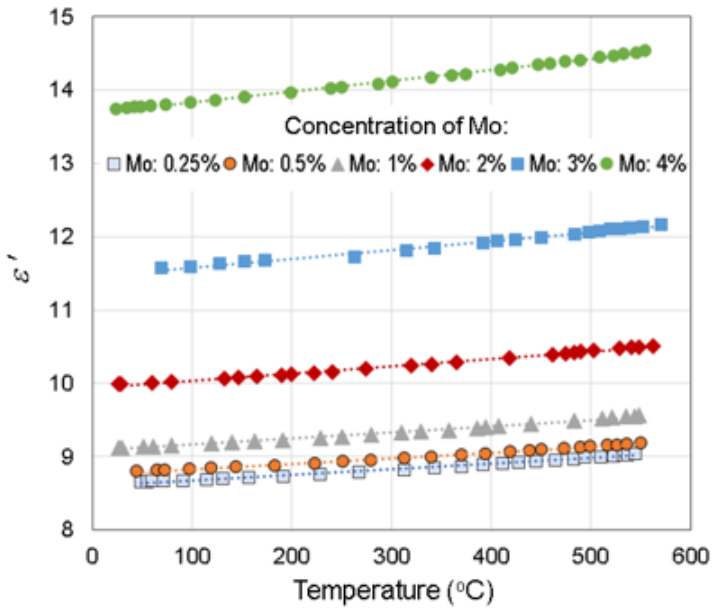

Figure 3.2: Data on measurement of dielectric constants for each concentration of Mo.

Table 3.1: Polynomial Approximations for the Dielectric Constant Values.

Mo Percent	Polynomial Approximation
0.25%	$y = 0.0008T + 8.5979$
0.5%	$y = 0.0008T + 8.7424$
1.0%	$y = 0.0008T + 9.0785$
2.0%	$y = 0.0010T + 9.9373$
3.0%	$y = 0.0012T + 11.458$
4.0%	$y = 0.0015T + 13.681$

3.2 AlN:Mo Composite: Experimental Data on Electromagnetic Parameters

Temperature characteristics of ε' and ε'' of the AlN:Mo samples were obtained with a dedicated apparatus for a free space dielectric measurement [32, 33] at 95 GHz for temperatures T up to 500-600°C. The measurements were carried out for six samples of AlN:Mo composite with Mo = 0.25, 0.5, 1.0, 2.0, 3.0, and 4.0%. The experimental results originally reported in [34] are presented in Figures 3.2 and 3.3.

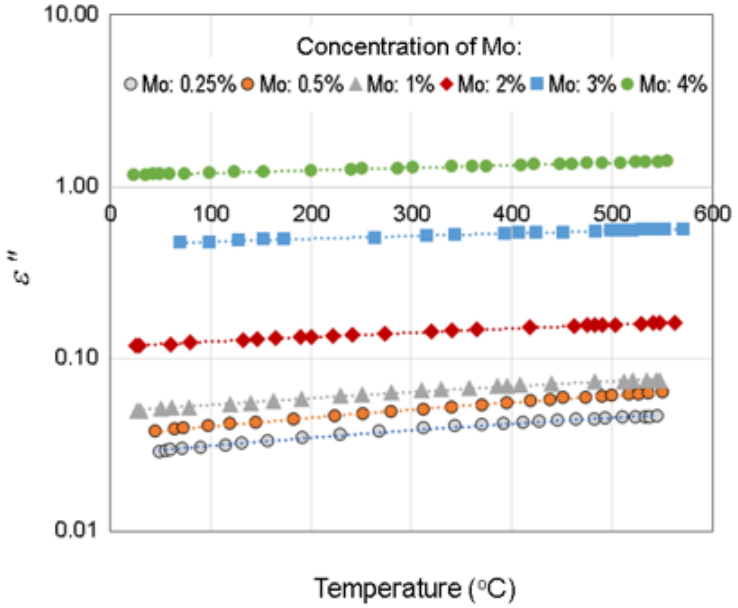

Figure 3.3: Data on measurement of loss factors for each concentration of Mo.

Table 3.2: Polynomial Approximations for the Loss Factor Values.

Mo Percent	Polynomial Approximation
0.25%	$y = 0.00004T + 0.0277$
0.5%	$y = 0.00005T + 0.0353$
1.0%	$y = 0.00005T + 0.0491$
2.0%	$y = 0.00005T + 0.1181$
3.0%	$y = 0.0002T + 0.4613$
4.0%	$y = 0.0004T + 0.1589$

Table 3.3: Density of the Ceramic Materials.

Mo Concentration	0.25%	0.5%	1.0%	2.0%	3.0%	4.0%
$\rho(\frac{g}{cm^3})$	3.32	3.33	3.37	3.44	3.50	3.57

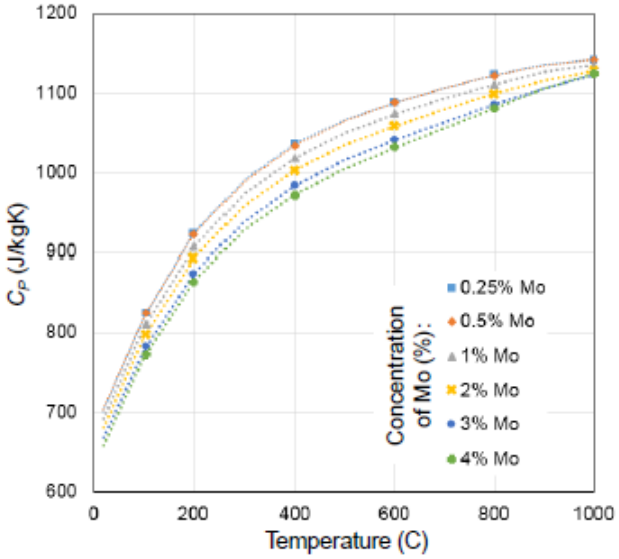

Figure 3.4: Polynomial approximations for new specific heat capacity values based on experimental data.

Table 3.4: Polynomial approximations for the updated specific heat capacity values.

Mo Percent	Polynomial Approximation
0.25%	$y = (-1E{-}09)x^4 + (3E{-}06)x^3 - 0.0033x^2 + 1.8372x + 666.21$
0.5%	$y = (-1E{-}09)x^4 + (3E{-}06)x^3 - 0.0032x^2 + 1.7904x + 669.15$
1.0%	$y = (-1E{-}09)x^4 + (3E{-}06)x^3 - 0.0031x^2 + 1.7621x + 657.7$
2.0%	$y = (-1E{-}09)x^4 + (3E{-}06)x^3 - 0.0031x^2 + 1.7351x + 647.3$
3.0%	$y = (-9E{-}10)x^4 + (3E{-}06)x^3 - 0.003x^2 + 1.6797x + 635.99$
4.0%	$y = (-1E{-}09)x^4 + (3E{-}06)x^3 - 0.0031x^2 + 1.7011x + 625.41$

It is seen that the experimental points for both dielectric constant and the loss factor form almost linearly increasing functions of temperature for all Mo concentrations. The values of ε'' are much larger for higher doping – with Mo = 4%, the loss factor is approximately 30 times higher than in the absence of the doping. However, as it turned out, ε' for higher percentages of Mo is also higher – for Mo = 4%, in approximately 1.5 times, if compared to Mo = 0.25%. This suggests that MMW heating of the composites with different Mo contents may occur very differently due to different distributions of the electric field. Therefore, this experimental data gives us an additional motivation for modeling the EM processes in the considered model of a MMW HX.

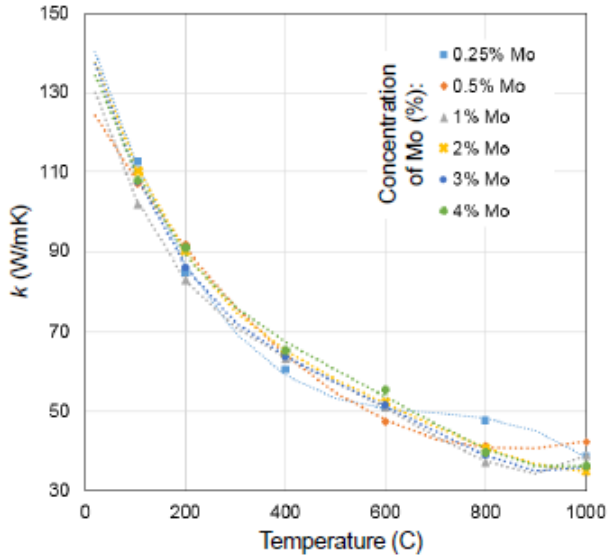

Figure 3.5: Polynomial approximations for new thermal conductivity values based on experimental data.

Table 3.5: Polynomial approximations for the updated thermal conductivity values.

Mo Percent	Polynomial Approximation
0.25%	$y = (-3E{-}07)x^3 + 0.0006x^2 - 0.4104x + 148.26$
0.5%	$y = (-1E{-}08)x^3 + 0.0001x^2 - 0.2163x + 128.43$
1.0%	$y = (6E{-}10)x^4 - (1E{-}06)x^3 + 0.0011x^2 - 0.4488x + 138.58$
2.0%	$y = (3E{-}10)x^4 - (8E{-}07)x^3 + 0.0008x^2 - 0.4052x + 145.34$
3.0%	$y = (5E{-}10)x^4 - (1E{-}06)x^3 + 0.001x^2 - 0.466x + 146.3$
4.0%	$y = (4E{-}10)x^4 - (1E{-}06)x^3 + 0.0009x^2 - 0.4006x + 142.2$

The experimental points in Figures 3.2 and 3.3 were approximated using the linear functions collected in Tables 3.1 and 3.2, respectively. Correspondence of the data to the linear functions appear to be adequate: the R^2 values for the polynomials are above 98%, indicating they are good fits for the data.

3.3 AlN:Mo Composite: Experimental Data on Thermal Parameters

Density ρ of AlN:Mo samples with variable Mo content were measured in [26] by the Archimedes method using methyl ethyl ketone as the fluid. The values of ρ were found to be a nearly linear function of Mo concentration. Using this function, in this paper, the density values are taken as shown in Table 3.3 and assumed to be temperature-independent.

Data on temperature characteristics of the specific heat capacity C_p of all six AlN:Mo composites in the interval from 100 to 1000°C was taken from [26] as shown in Figure 3.4. In the referenced paper, the points were calculated, using the mixture models, for 6 particular temperatures; to verify the calculations, samples of three compositions (Mo = 0.25, 0.5, and 1.0%) were measured using differential scanning calorimetry in which uncertainty of C_p values was within 5% in the interval from 30 to 600°C. While the data points show no strong dependence on Mo concentration, it is seen that the heat capacity significantly increases with temperature.

In order to get functions approximating characteristics of C_p for all six samples in the entire temperature range, the experimental points in Figure 3.4 were interpolated by polynomials of order 4 as shown in Table 3.4.

Data on temperature characteristics of thermal conductivity k of all six materials in the interval from 100 to 1000°C was also taken from [26]; the data points are shown in Figure 3.5. In the referenced paper, the values of k were calculated (with uncertainty estimated to be within 10%) from experimental data on thermal diffusivity, which was measured by the laser flash method. The data points also show no strong dependence on Mo concentration, but reveal strong decrease of thermal conductivity with temperature.

Functions approximating characteristics of k were obtained by interpolating the data points by polynomials of orders 3 and 4 as shown in Table 3.5.

Chapter 4

Computational Model

Aiming to help design the first physical prototype of a MMW HX, we report here a computer model capable of simulating EM and (EM-induced) thermal processes in a single ceramic block of the system that is irradiated by a plane wave and attached to a thin metal plate. An ultimate goal of the computational experiments is to evaluate the applicability of an AlN:Mo composite as a susceptor material and find the composition that absorbs maximum MMW power and, at the same time, produces satisfactorily uniform temperature distribution on the back surface.

4.1 The FDTD Model

A model created in the *QuickWave* environment intends to simulate heating a single ceramic block with a metal plate on the back surface. The height and width of the block, denoted as a in Figure 4.1, are both 10 mm, while the thickness, denoted by t, ranges from 8 to 12 mm. The thickness of the metal plate, denoted as b, is set to 1mm. The incident field has a frequency of 95GHz, with the power set to either 30W or 100W. Six different concentrations of Mo, 0.25%, 0.5%, 1.0%, 2.0%, 3.0%, and 4.0%, are investigated in the following computational experiments, and the heating temperature ranges from 20 to 1000°C.

Corresponding polynomial approximations shown in Tables 3.1-3.5 are used to generate the values of ε', ε'', C_p, and k at 20, 100, 200, ..., 1,000°C as tabulated input data for the coupled model. The step of 100°C is chosen to guarantee adequate representation of temperature characteristics of all material parameters.

To imitate the incoming plane wave and the absorbing boundary conditions making the

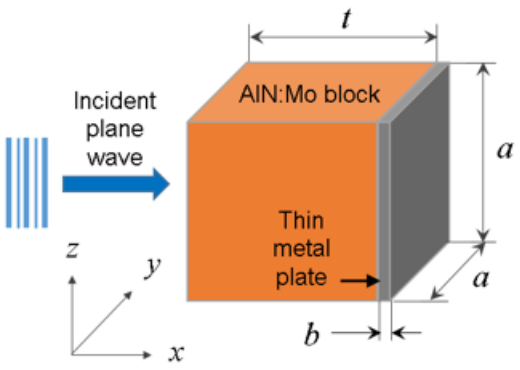

Figure 4.1: Rectangular AlN:Mo susceptor with a metal plate attached to the back surface - the scenario reproduced in the model.

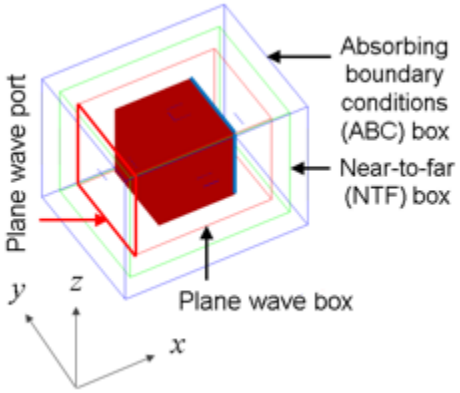

Figure 4.2: EM boundary conditions in the model.

spatial domain around the ceramic and metal objects finite, the AlN:Mo block is surrounded by the 18x13x13 mm plane wave box with one 13x13 mm face responsible for sinusoidal excitation of the incident field. This box is situated inside the 24x19x19 mm box imitating the Mur with superabsorption boundary condition [22] as shown in Figure 4.2.

Simulations are performed on a Windows 10 workstation with two Intel Xeon Gold 5120 processors with a base/peak frequency of 2.2/3.2 GHz (each having 14 cores and supporting 28 threads), the GPU NVIDIA Quadro P5000, and 1 TB RAM.

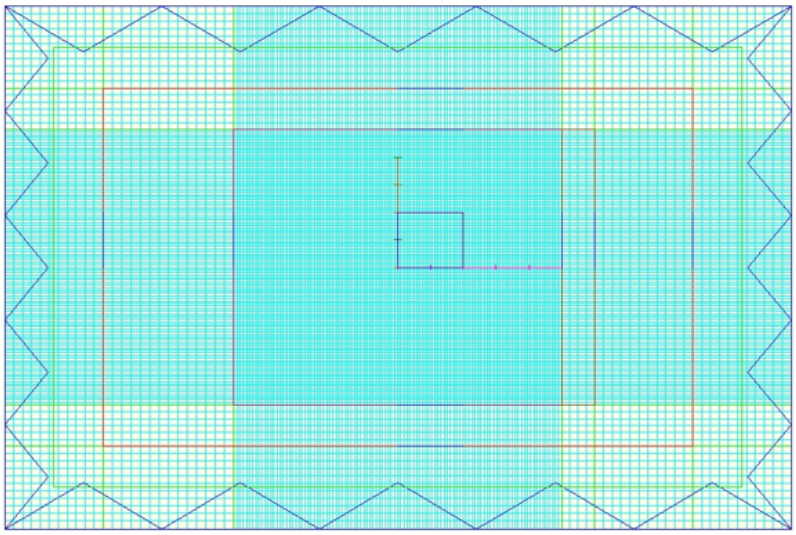

Figure 4.3: FDTD mesh in the model.

The mesh created in the model is shown in Figure 4.3; it has, depending on Mo content, between 6.2 and 10.8 million FDTD cells and takes from 593 to 1025 MB of RAM. The mesh is non-uniform, being more dense in the ceramic block than in the surrounding air. The maximum cell size is 0.290mm for air and from 0.075 to 0.095mm for the AlN:Mo block, depending on the concentration of Mo. Since the dielectric properties of the material are temperature-dependent, the cell sizes in the block needed to be chosen in accordance with FDTD norms in order to ensure at least 10 cells per wavelength. When temperature rises, so does ε', meaning the wavelength in the ceramic material shortens, which in turn would require a smaller cell size in the mesh. The experimental data compiled from Figures 3.2 and 3.3 and listed in Table 4.1 were used to calculate the cell sizes necessary to maintain accurate results. Those cell sizes, discretized by 10, 15, and 20 cells/wavelength, are shown in Table 4.2, with cell size calculated for 20 and 1000°C. The maximum cell size in the mesh for the AlN:Mo block was chosen to have 11 cells/wavelength, and corresponds to the value for 1000°C for each material.

Table 4.1: Dielectric Properties of the Ceramic Materials at 20 and 1000 C at $f = 95$ GHz.

Material	Temp (°C)	ε'	ε''	σ (S/m)
AlN:Mo 0.25%	20	8.61	0.0285	0.1504
	1000	9.40	0.0677	0.3573
AlN:Mo 1.0%	20	9.09	0.0501	0.2644
	1000	9.88	0.0991	0.5230
AlN:Mo 4.0%	20	13.45	1.1669	6.1587
	1000	14.73	1.5381	8.1176

Table 4.2: Sizes of FDTD Cells (in mm) in the Model Operating at $f = 95$ GHz.

Cells per wavelength	Air	AlN 0.25%		AlN 1.0%		AlN 4.0%	
Temp (°C)		20	1000	20	1000	20	1000
10	0.32	0.109	0.104	0.106	0.102	0.087	0.083
15	0.21	0.072	0.068	0.069	0.067	0.057	0.055
20	0.16	0.055	0.052	0.053	0.051	0.044	0.042

4.2 Input Data for the EM-Thermal Model

In order to model the EM-thermal coupled scenario, *QuickWave* requires seven parameters to be inputted into a *.pmo file. The first two parameters are the full temperature range for the simulation being performed and the corresponding enthalpy at the corresponding temperatures. The electromagnetic parameters specified are the dielectric constants and loss factors at each temperature. The thermal parameters are the specific heat capacity, thermal conductivity, and density, also for each temperature. *QuickWave* assumes a linear relationship to determine unknown values for each parameter for temperatures between the ones specified in the *.pmo file. Figure 4.4 shows the *.pmo files for each concentration of Mo.

```
# AlN:Mo 3.0% composite media file for QW-BHM module (Nov 2018 SAM & VVY)
# Measurements by AFRL-Kirtland, Albuquerque, NM
# Post-processing of measured data by IMMG/CIMS/WPI, Worcester, MA
# DATA FROM 20 C to 1000 C
```

!Temperature	Enthalpy	EPa	SIGa	SpecHeat	Density	Ka
# C	J/cm3		S/m	J/gC	g/cm^3	W/cmC
20	0	11.48	2.4558	0.668	3.50	1.3739
100	202.4	11.58	2.5402	0.777	3.50	1.0899
200	491.3	11.70	2.6458	0.874	3.50	0.8615
300	808.5	11.82	2.7513	0.939	3.50	0.7249
400	1145.0	11.94	2.8569	0.983	3.50	0.6389
500	1494.8	12.06	2.9624	1.015	3.50	0.5741
600	1854.5	12.18	3.0680	1.040	3.50	0.5129
700	2222.7	12.30	3.1735	1.063	3.50	0.4492
800	2598.6	12.42	3.2791	1.085	3.50	0.3888
900	2982.0	12.54	3.3847	1.106	3.50	0.3491
1000	3372.0	12.66	3.4902	1.123	3.50	0.3594

Figure 4.4: Input data for the FDTD coupled EM-thermal model in *QuickWave* for 3.0% Mo.

4.3 Thermal Boundary Conditions

In this Thesis, we consider two scenarios with different thermal boundary conditions. The first one applies Neumann (adiabatic) conditions on all boundaries of the susceptor, i.e., on the ones between the ceramic and air as well as between the ceramic and the metal plate. These conditions imitate full thermal insulation of the ceramic block; they are considered in order to see the full effect of MMW heating without any loss to the surroundings.

The second scenario applies a Dirichlet (explicit) condition on the boundary between the ceramic block and the metal plate; all other boundaries in the system have Neumann conditions. This scenario imitates a practical regime in operation of a MMW HX. When the temperature of the heated ceramic block reaches a certain level, T_c, the temperature of the metal plate becomes fixed (using some external mechanisms) and is maintained constant. In this case, the metal plate produces a cooling effect on the block, which continues to be heated by the incoming MMW field; in some time, the temperature in the block is expected to reach equilibrium with a non-uniform temperature distribution throughout the volume – maximum on the front surface, minimum on the back surface adjacent to the metal plate.

This regime is implemented in the model using special manipulations of *QuickWave*'s *.pm2 files (see Appendix C).

Table 4.3: Parameters of the Test Scenario for Benchmarking of the FDTD Model.

Frequency (GHz)	Power (W)	Ceramic block (mm)	Metal plate (mm)	ε'	ε''
2.45	100	100x100x100	100x100x10	6.69	0.19

4.4 Benchmarking of the FDTD Model Against a COMSOL Model

Experimental validation of the thermal FDTD model is not currently possible, so to benchmark the FDTD model created in the *QuickWave* environment, its EM output is compared to the one produced by a finite element EM frequency-domain model built in *COMSOL Multiphysics* [35]. Due to computational constraints (RAM and CPU), it is not possible directly reproduce the scenarios of the FDTD model in *COMSOL*. Therefore, the FDTD and FEM models are applied to the system in Figure 4.1 at the microwave frequency range with the parameters listed in Table 4.3.

The ceramic block is assumed to be made of zirconia; its complex permittivity at 2.45 GHz is taken from [24]. In this test, the FDTD mesh is built with a maximum cell size of 6 and 2 mm in air and zirconia, respectively. With the ABC box of 240x190x190 mm, the total number of cells is 152,880, meaning there are more than 11 cells per wavelength. The FDTD model only uses 15 MB of memory.

The FEM model in *COMSOL Multiphysics* uses a single box for both plane wave excitation (by the face in the yz-plane) and for setting a finite domain around the system with an absorbing boundary condition on its boundaries; the latter is implemented using the principles of a Perfectly Matched Layer. The domain is the same size as that of the FDTD model. The 3D mesh of quadratic tetrahedral elements is built under the condition of 10 elements per wavelength [36][37], exceeding the finite element convention of 6 [38], for a total of 288,797 elements. The resulting FEM model requires at least 11.9 GB of memory to run, which is significantly more than the FDTD model.

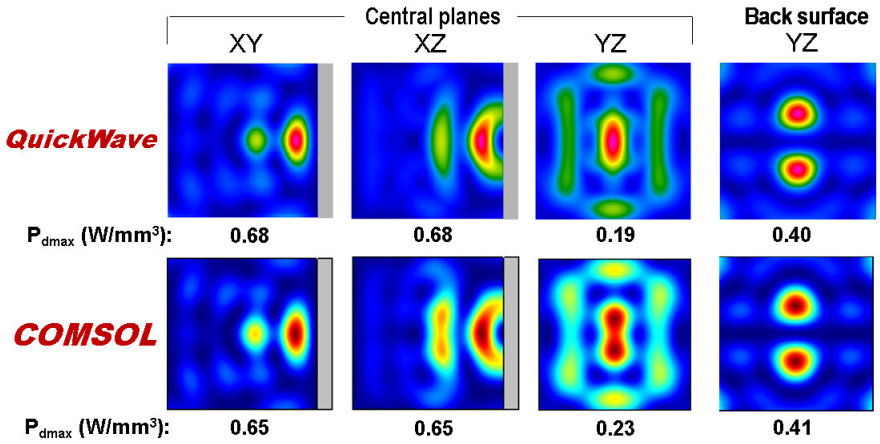

Figure 4.5: Comparison of patterns of density of dissipated power: the FEM (*COMSOL Multiphysics*) and FDTD (*QuickWave*) models.

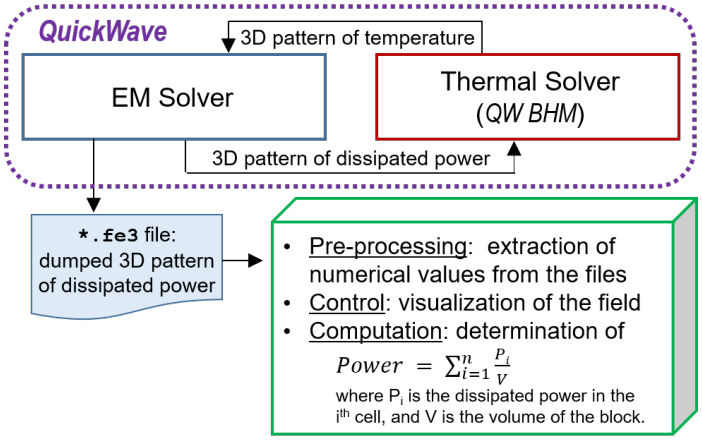

Figure 4.6: Diagram of the visualization procedure for MATLAB.

2D patterns of dissipated power in the zirconia block that are produced by both models are shown in Figure 4.5. The field distributions seem to be almost identical, and the maximum values of dissipated power in the corresponding patterns are very close. These similarities provide an additional degree of confidence about the adequacy of the developed FDTD model.

4.5 Post-Processing Data of Dissipated Power with MATLAB

For alternative visualization and quantitative characterization of patterns of dissipated power, the output files produced during a *QuickWave* simulation can be post-processed in the MATLAB environment. A special script was written to read *.fe3 files containing dissipated power data and

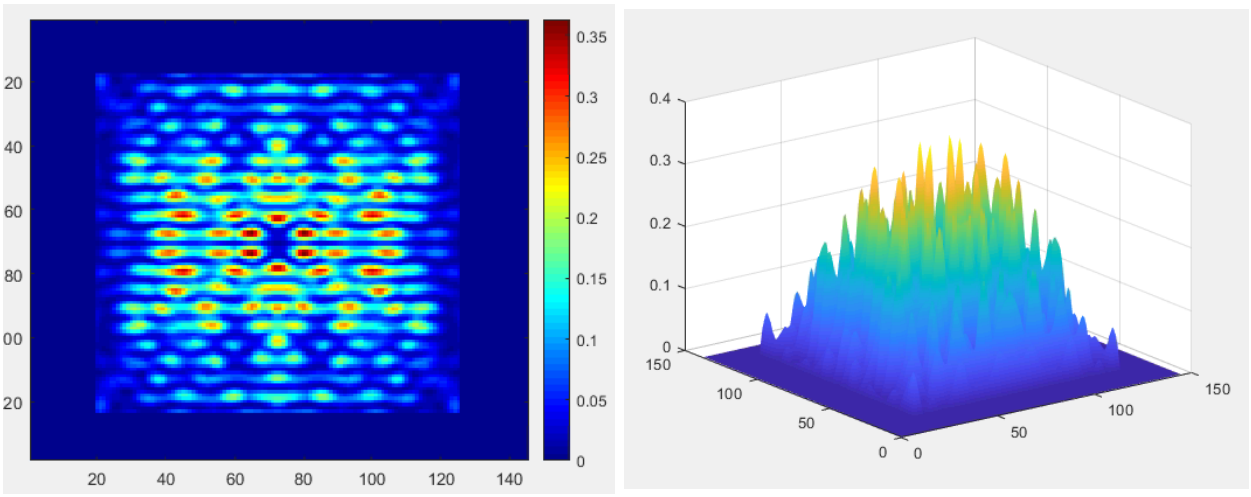

(a) (b)

Figure 4.7: Examples of 2D and 3D MATLAB visualizations of dissipated power in a particular plane of the ceramic block.

to visualize the patterns using a variety of MATLAB graphics tools. The algorithm of the visualization process is outlined in Figure 4.6. Currently, the script produces two types of plots representing a pattern. Examples of visualizations are shown in Figure 4.7. In addition to the graphical functions, the script can also perform certain calculations with the dissipated power values. The code is presented in Appendix A.

Chapter 5

Thermal Processes under Full Thermal Insulation of the AlN:Mo Susceptor

5.1 Ceramic Block without a Metal Plate

In the first computational scenario a thin metal plate on the back surface of the ceramic block is not present. This setup allows us to observe propagation of the MMW plane wave through the AlN:Mo sample. Patterns of dissipated power density in the central coordinate planes and on the back surface of the block are shown in Figure 5.1. It is seen that when an AlN:Mo block is hit by a MMW plane wave, patterns of dissipated power in the materials, regardless of the contents of Mo, are characterized by multiple maxima/minima. The quantity of "hot spots" spread over the area of 10 x 10 mm size suggests that, due to high thermal conductivity in the AlN:Mo composites, the block may be heated sufficiently uniformly.

Uniform heating of the block is another requirement for the MMW HX. Temperature fields in the AlN:Mo block are computed with the coupled EM-thermal model. Figure 5.2 characterizes the heating process of all six composite samples from 20 to 1000°C. It is seen that, when the power of the incoming wave is 100 W, taking, depending on the Mo content, from 50 to 110 s, the minimum and maximum temperatures in the block remain very close during the entire process. This indicates a high level of uniformity of temperature throughout the block. Samples with higher concentration

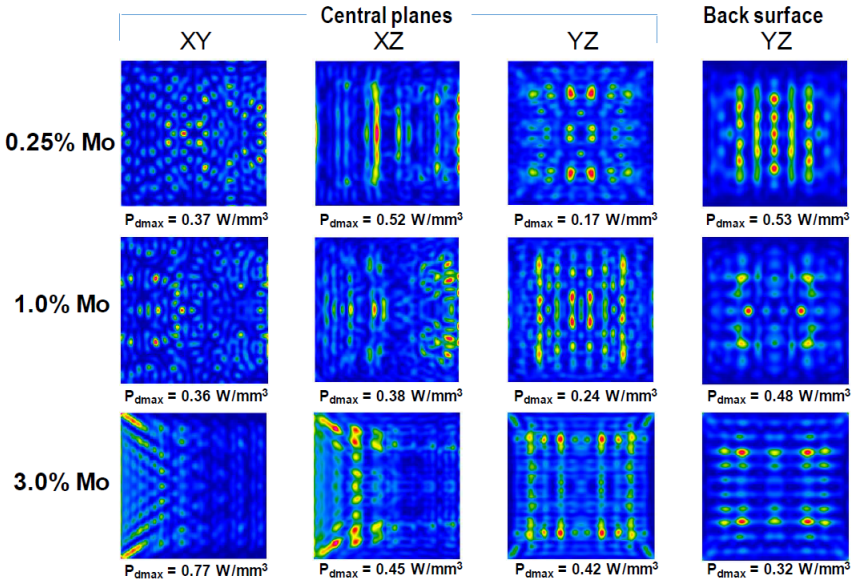

Figure 5.1: Patterns of density of dissipated power in the absence of the metal plate and full thermal insulation of the AlN:Mo block at $T = 20$°C; maximum value of P_d is shown under each pattern; power of incoming plane wave $P = 100$W.

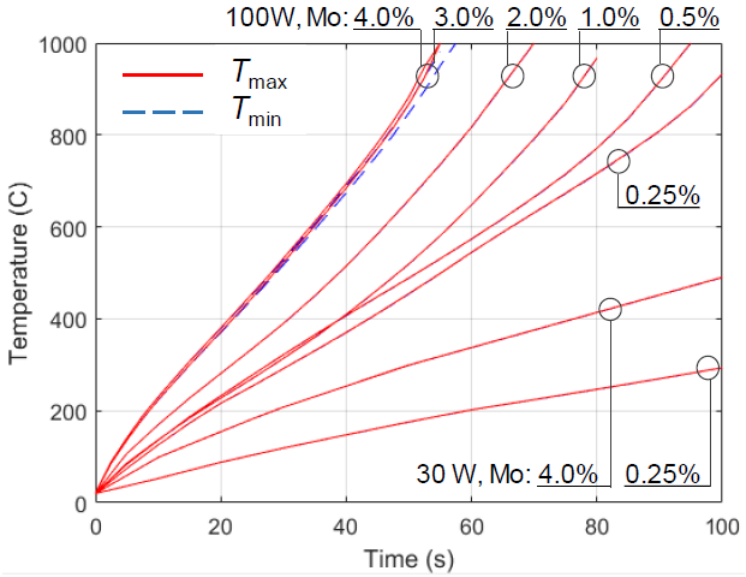

Figure 5.2: True characteristics of minimum and maximum temperatures in the AlN:Mo block; no metal plate; $P = 30$ and 100W.

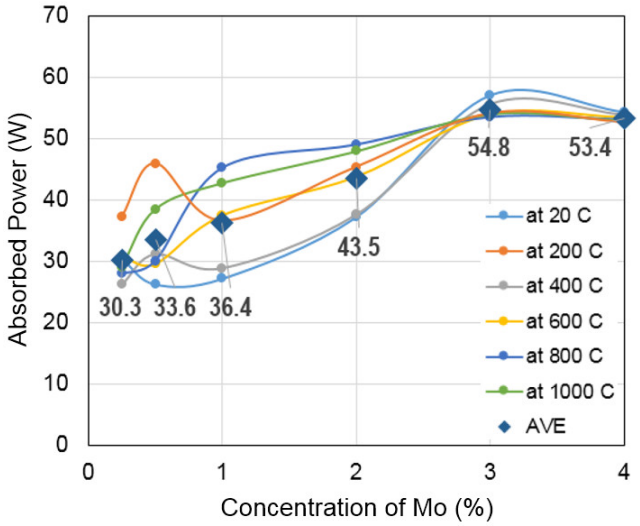

Figure 5.3: Total power absorbed at different temperatures of the AlN:Mo block; no metal plate; $P = 100$W.

of Mo are heated faster because those composites are characterized by higher dielectric losses (Section 3.2). When the power is 30 W, the samples are also heated very uniformly, though the heating rate is 2-3 times lower.

Comparing the patterns in Figure 5.1 with the graphs in Figure 5.2, one can conclude that a high level of temperature uniformity in the AlN:Mo sample is ensured by a high level of thermal conductivity (Section 3.2) which allows the multiple "hot spots" to spread throughout the volume.

Energy efficiency of the block is one of the requirements for the MMW-powered HX. Absorbed power, computed as a function of Mo concentration, is shown in Figure 5.3. For higher concentrations of Mo we observe less variation in absorbed power between temperatures. The block with 3% Mo is characterized by the highest average absorbed power, indicating the highest energy efficiency.

5.2 Patterns for Dissipated Power Density

Compared to the case of no metal plate on the back surface of the AlN:Mo block (Section 5.1), when the plate is present, distributions of dissipated power in the ceramic samples are different because of an impact of that plate producing a reflected wave propagating back to the front surface of the sample. Two groups of patterns computed for low (20°C) and high (800°C) temperatures of the block are shown in Figure 5.4. The patterns look alike for the highest concentrations of Mo, but

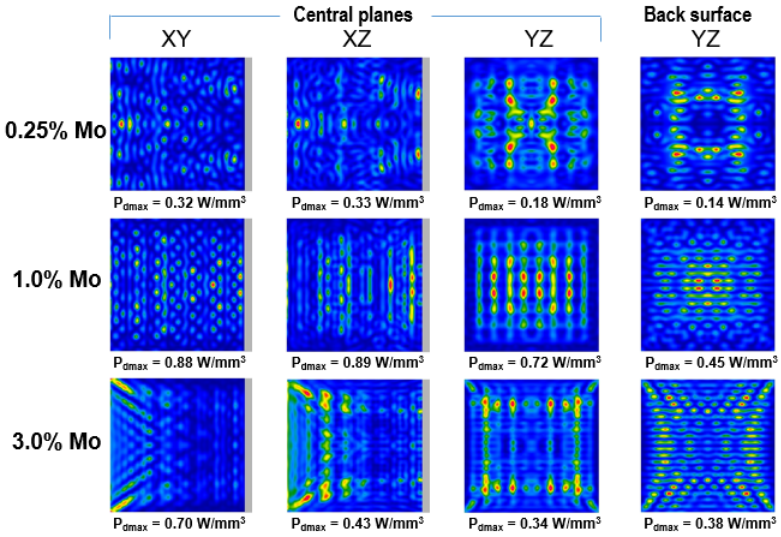

(a)

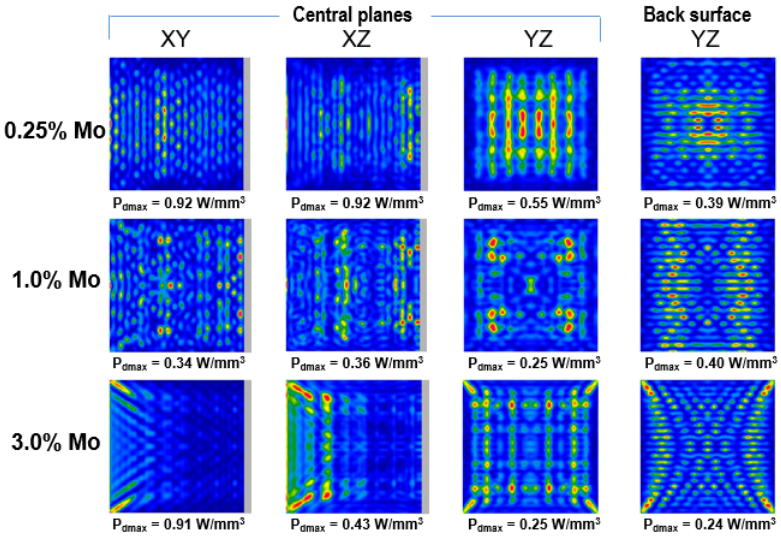

(b)

Figure 5.4: Patterns of dissipated power density in the presence of the metal plate on the back surface and with full thermal insulation of the AlN:Mo block with Mo = 0.25, 1.0, and 3.0% for the block's temperature of 20°C (a) and 800°C (b); $P = 100$ W.

are very different for the lower concentrations; this can be explained by the presence of the reflected wave which is more influential in the samples with lower dielectric losses. Multiple hot spots are still spread throughout the block, indicating that there is also potential for uniform heating of the block in this case. The back surface of the sample is characterized by a uniform distribution of hot spots for all concentrations of Mo.

5.3 Time Evolution of Temperature Fields

Temperature fields varying in the course of heating of the AlN:Mo blocks were computed with the use of the coupled EM-thermal model. Temperature patterns shown in Figure 5.5 represent the process in all six AlN:Mo samples. The patterns are visualized here for the back surface of the block, which is important for knowing temperature distribution from the viewpoint of system design. However, since all the modeling results are 3-dimensional, temperature patterns in other planes were also evaluated and found equally uniform.

For each concentration of Mo one can observe a very high level of spatial heating uniformity; this phenomenon can be contributed to the elevated level of thermal conductivity of the composites. In accordance with the data in Figure 3.5, the values of k are high for all the materials, and they decrease synchronously with temperature for all concentrations of Mo. This makes the heating processes in all samples (as they are shown in 5.5) very similar in terms of heating uniformity.

It is also seen that the composite block with higher concentrations of Mo is heated notably faster: for instance, the block with Mo = 0.25% reaches the temperature of 604°C within 70 s, whereas it takes 50 s to heat the sample with Mo = 4.0% up to 818°C. Higher dielectric losses of the composites with higher Mo content are responsible for this behavior.

Time-temperature characteristics of the minimum and maximum temperatures in all six samples are shown in Figure 5.6. The curves confirm the results of Figure 5.5: temperature distributions are highly uniform at all stages of the heating process. Similarly to the case of the absent metal plate, heating rates for the lower power (30 W) are much lower. For 100 W, the samples are heated up to 1,000°C for, depending on their concentrations of Mo, 60 to 95s. The times here are different from the ones in Figure 5.2, and that is clearly explained by the impact of the metal plate producing the reflected wave which contributes additional heat to the composite block.

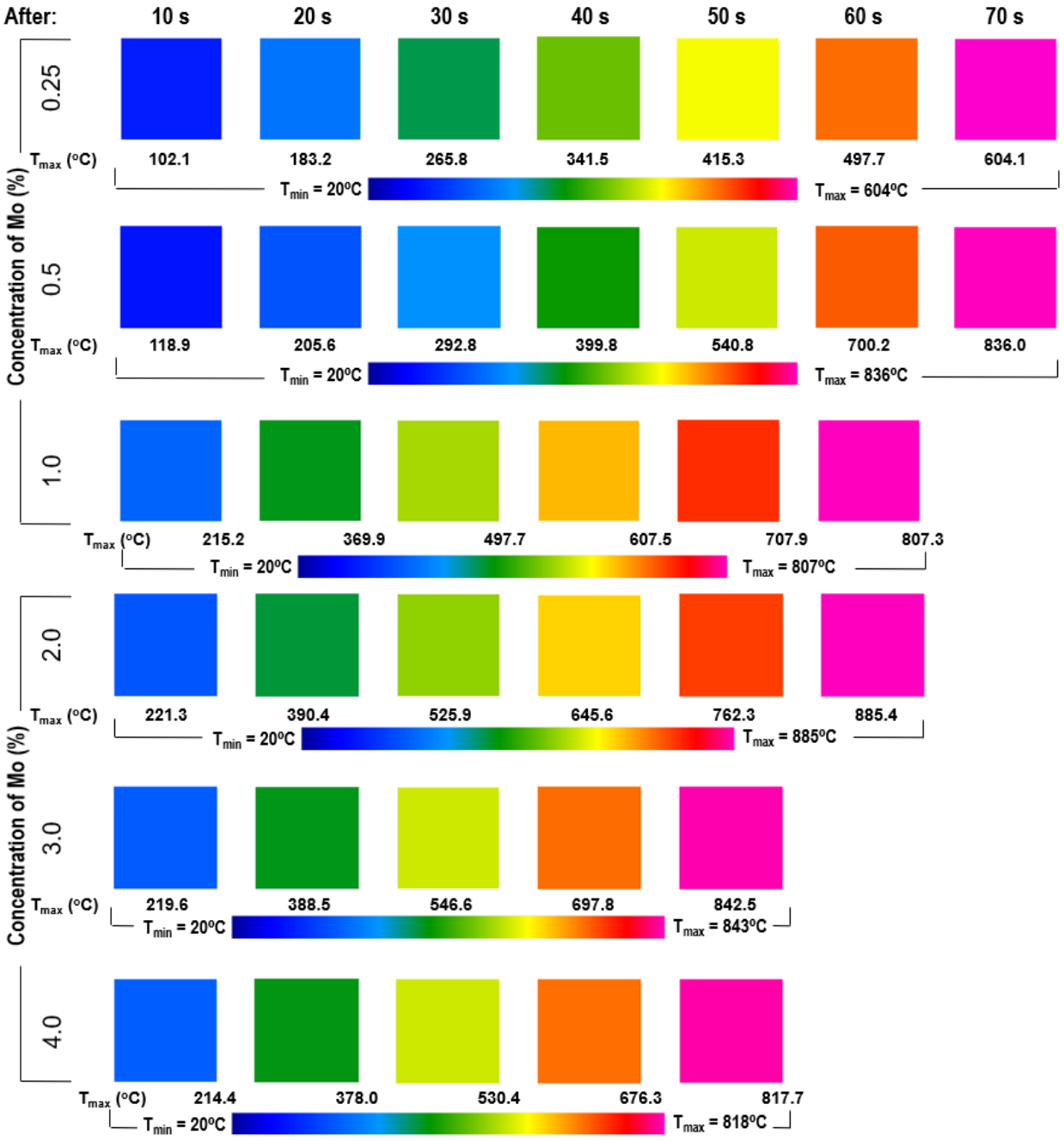

Figure 5.5: Temperature distributions on the back surface (YZ-plane) of the AlN:Mo block with Mo = 0.25, 0.5, 1.0, 2.0, 3.0, and 4.0% along with maximum values of temperature (T_{max}) in each pattern. Patterns are normalized to the minimum temperature of the process (20°C); heating time steps are 5 (Mo = 0.25 and 0.5%), 2.5 (Mo = 1.0 and 2.0%), and 2.0 s (Mo = 3.0 and 4.0%); P = 100 W; t = 10 mm.

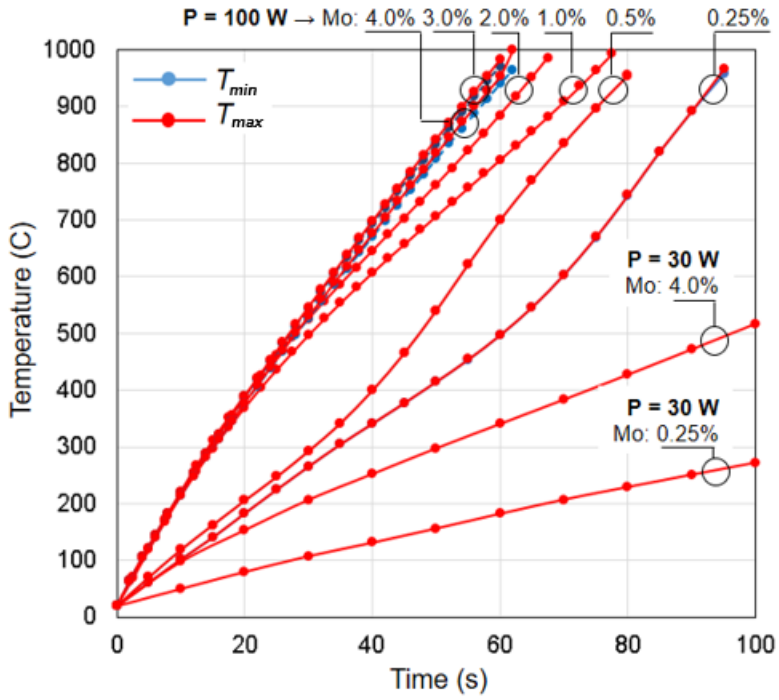

Figure 5.6: Time characteristics of minimum and maximum temperatures in the AlN:Mo block; full thermal insulation; $P = 30$ and 100W.

5.4 Results for Total Dissipated Power

A fraction of power of the upcoming MMW that is absorbed by the AlN:Mo composite was computed for different temperatures of the composite block. This computation requires EM modeling, so temperature as a parameter of the sample was introduced through the EM material parameters (dielectric constant ε' and the loss factor ε'') at particular temperatures. This approach appears to be feasible because, as shown in Figure 5.6, the temperature distribution in the volume of the block throughout the heating process is highly uniform; this ensures uniformity of the distribution of material parameters throughout the volume of the sample.

The curves in Figure 5.7 suggest that, for low Mo concentrations, total absorbed power is fairly different at different temperatures, but for high contents of Mo (3-4%), the values converge to the maximum values for all temperatures. Accordingly, the average absorbed power for all temperatures is also the highest for Mo~3%.

Computed data for total absorbed power allows us to evaluate energy efficiency of the considered MMW HX and thus evaluate the operation of the system against another key characteristic of

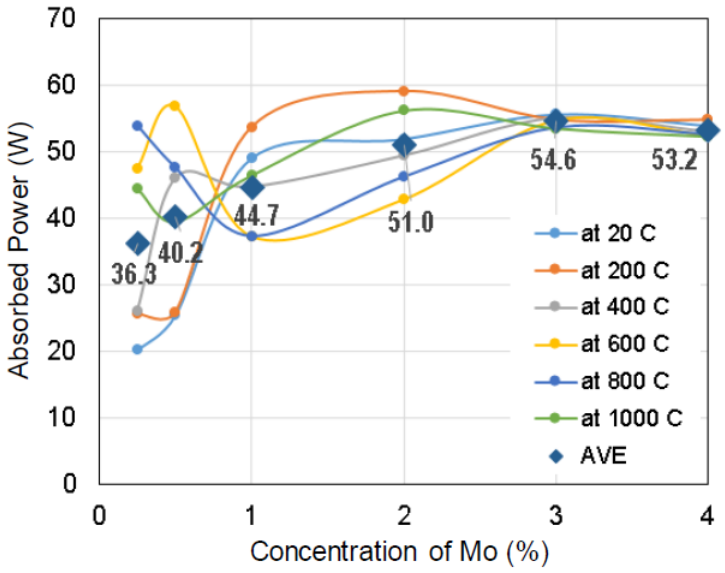

Figure 5.7: Total power absorbed at different temperatures of the AlN:Mo block; thin metal plate on back surface; $P = 100$W.

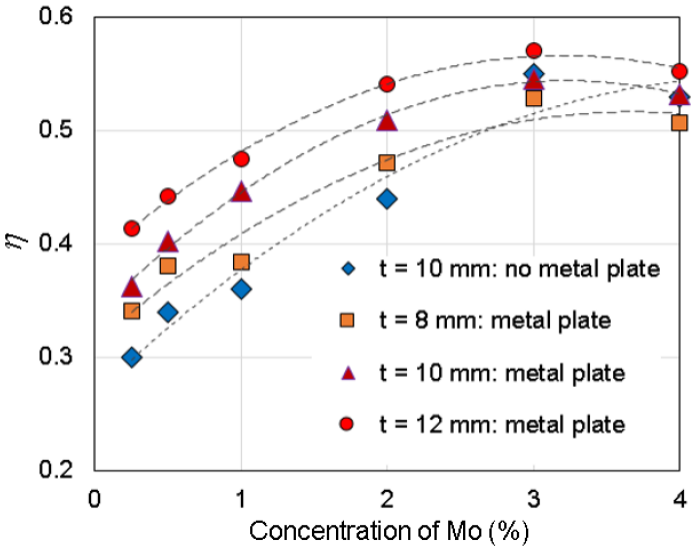

Figure 5.8: Energy efficiency of the block with and without a metal plate.

the device. We introduce the parameter:

$$\eta = \frac{P_d}{P},$$

where P_d is the power dissipated in the ceramic material and P is the power carried by the incoming plane wave, as a measure of energy efficiency of the heating process in the MMW HX. In Figure 5.8, we show the characteristics of η as functions of Mo content for different thicknesses of the sample (8, 10, and 12 mm) not only with the metal plate on the back surface, but also, for the case of $t = 10$ mm, in the absence of the metal plate. It is seen that with no reflected wave in the sample, energy efficiency grows nearly linearly with the growth of concentration of Mo. However, with the metal plate attached to the back surface, energy efficiency tends to have a maximum for Mo around 3%.

Chapter 6

Thermal Processes under the Condition of Constant Temperature on the Back Surface

The real world heat exchanger will have the ceramic blocks and metal plate heat until reaching a desired temperature and then hold the metal plate at that temperature using some external mechanisms in order to prevent overheating the blocks. Mimicking, with a sufficient degree of adequacy, such a regime in a computer model is a central goal of the initial stage of the computational study of the MMW HX. However, there is no readily available option in the *QuickWave* environment for setting and maintaining constant temperature on the metal plate in the middle of the iterative procedure of solving the coupled EM-thermal problem.

The following approach was developed in this Thesis to resolve this issue. It appears that, due to the uniformity of the temperature distributions in the block in the course of MMW heating, the simulation can start at the desired high temperature T_c rather than at the initial room temperature of the process. In this case, the iterative procedure of solving the EM-thermal coupled problem (described in Section 4.1) can work from the very beginning with:

(a) material parameters in the input data (i.e., in the *.pmo files) corresponding to the high temperature T_c, and

(b) an explicit (Dirichlet) thermal boundary condition setting the high constant temperature T_c on the interface between the back surface of the AlN:Mo block and the metal plate.

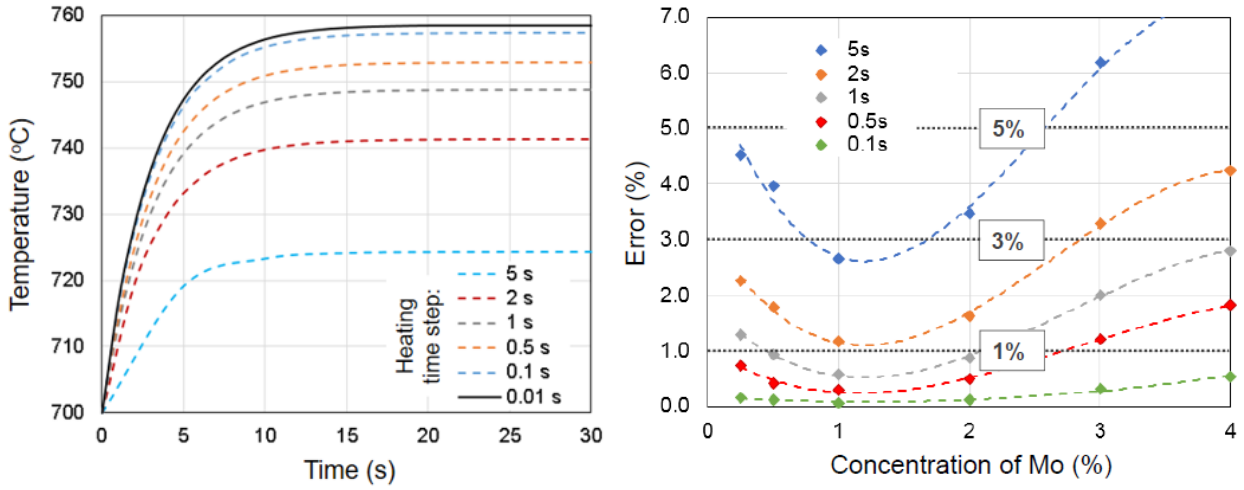

(a) (b)

Figure 6.1: Maximum temperature in the block for different heating time steps with metal plate held at constant 700 C for 0.25% Mo and $P = 100$W (a); error for heating time steps with respect to 0.01s for all concentrations (b); Mo = 0.25%, $T_c = 700$°C, $P = 100$W.

This approach was implemented in a special version of the FDTD model through the appropriate application of *QuickWave*'s *.pm2 files (presented in Appendix C). Computational results in this Chapter are obtained with the use of that version of the model.

6.1 Effect of Heating Time Step in the FDTD Model

While simulating the effect of holding the metal plate at T_c, it became apparent that the computed temperature fields are different depending on the heating time step (HTS) Δt. Normally, the HTS is chosen to follow the temperature-dependent material parameters (collected in the *.pmo file, Figure 4.4) in such a way that the computed maximum temperature falls into the same temperature step in the input data (first column in the *.pmo file) at least once. However, the HTS's which were sufficient in the model with a Neumann thermal boundary condition on the interface with the metal plate resulted in notably different time-temperature characteristics of maximum temperature of the block in this scenario.

A smaller HTS turned out to be necessary to get accurate results. Decreasing the time step led to an eventual convergence of the maximum temperature, as shown in Figure 6.1(a) for the composite with particular Mo concentration (0.25%) and $T_c = 700$°C. With the power of the

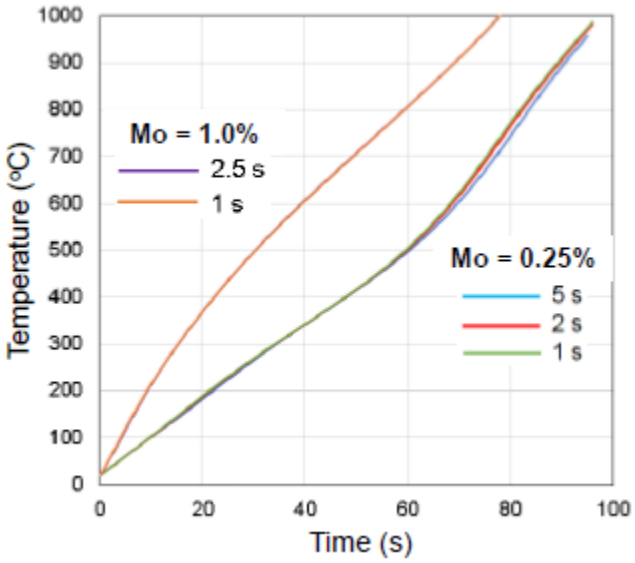

Figure 6.2: Maximum temperature in the block for different heating time steps with full thermal insulation for both 0.25% and 1.0% Mo at $P = 100$W.

incoming plane wave of 100 W, for all HTS, the maximum temperature reaches saturation after about 15s of heating, but the levels of those saturations are remarkably different. The accurate solution seems to correspond to a very small HTS (0.01 s) which is very computationally extensive.

In order to determine the levels of practical accuracy in the required computational study, we computed the errors (corresponding to different HTS's) as functions of Mo content; these characteristics are shown in Figure 6.1(b). It appears that in order to get the accuracy of 5% error for the materials with Mo $>$ 0.25%, the HTS of 5s might be sufficient. However, for 1% error in the sample with Mo = 1%, the HTS should be less than 2s.

It is worth emphasizing that such a strong dependency on the HTS was not observed in the model with the Neumann thermal boundary condition, i.e., in the case of full thermal insulation of the sample. Examples of the time-temperature characteristics of the heating processes in the Neumann case are shown in Figure 6.2. It appears that the observed HTS effect takes place only when the back surface of the block is kept at some constant temperature T_c. The Dirichlet boundary condition produces non-uniform (along the x-axis) temperature distributions. For example, for T_c = 700°C and the composite with Mo = 0.25%, the temperature gradient in equilibrium is about 60°C. This degree of non-uniformity is apparently enough to produce the observed HTS effect.

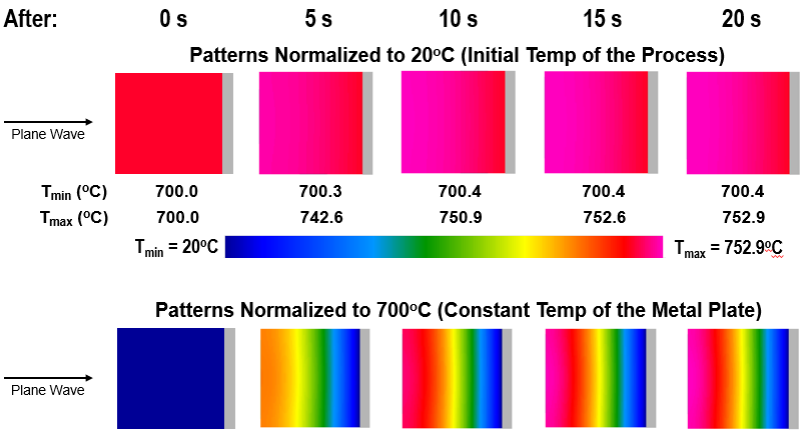

(a)

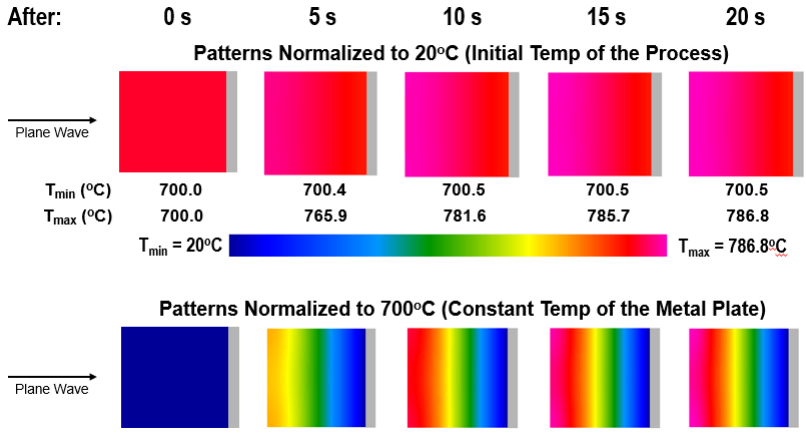

(b)

Figure 6.3: Normalized temperature patterns in the block in the central XY-plane with metal plate held at constant 700 C for Mo = 0.25% (a) and Mo = 3.0% (b) with $P = 100$W.

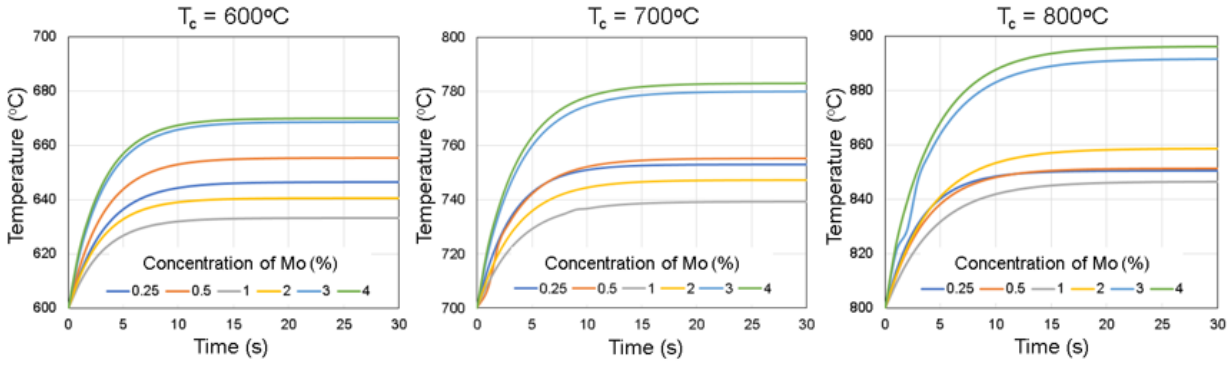

Figure 6.4: Maximum temperature in the block for different concentrations of Mo with metal plate held at constant 600, 700, and 800 C for $P = 100$W.

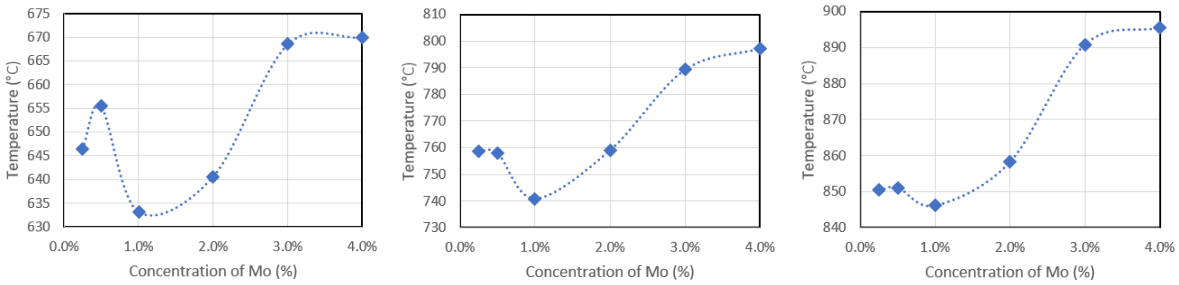

(a) (b) (c)

Figure 6.5: Maximum temperature in the block with $P = 100$W and metal plate held at constant (a) 600 C (b) 700 C and (c) 800 C for all concentrations of Mo.

6.2 Time Evolution of Temperature Fields

With the accuracy of simulation not under control, the temperature distribution along the x-axis is now illustrated in Figure 6.3 as 2D patterns visualized in two alternative modes. The patterns show the temperature distributions in the XY-plane for two different Mo contents (0.25 and 3.0%) over the course of 20s of heating when the metal plate is held at 700°C.

It is seen that adding the boundary condition with the constant temperature of the metal plate causes the maximum temperature to vary in a nonlinear pattern. The maximum temperature is established on the front surface (directly irradiated by the plane wave) whereas the minimum temperature is maintained on the back surface (due to the temperature of the metal plate being held constant). Figure 6.4 shows the time-temperature characteristics of the maximum temperature for different Mo concentrations; three different values of T_c (600, 700, and 800°C) are considered. There is less variation in temperature between materials when the plate is held at a lower temperature, but with the metal plate at 800°C the temperature gradient does not exceed 100°C.

Figure 6.5 contains the curves derived from the results presented in Figure 6.4: maximum temperatures of the block as functions of Mo contents for $T_c = 600$, 700, and 800°C. It is seen that the composite with 1.0% of Mo is heated the slowest and has the lowest maximum temperature while the composite with 4.0% of Mo is heated the fastest and reaches the highest temperature overall.

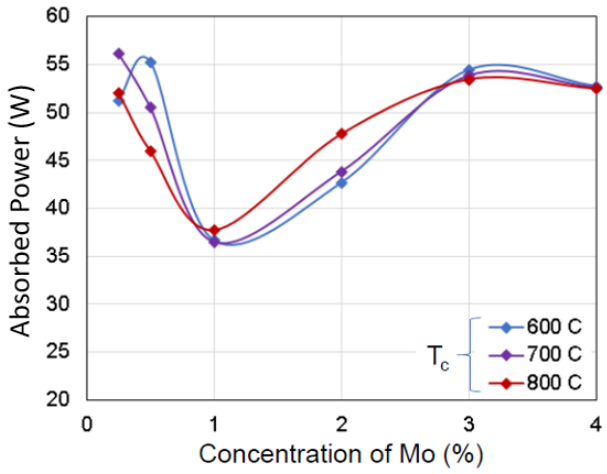

Figure 6.6: Absorbed power in the block when the plate is held at T_c = 600, 700, and 800°C with P = 100W.

6.3 Total Dissipated Power

Power absorbed in the ceramic block was simulated to determine the most efficient concentration of Mo. The total dissipated power remains relatively constant over time, so the average over 20s of heating was used to determine efficiency. Computations were done with the metal plate held at 600, 700, and 800°C, as shown in Figure 6.6. While 0.25% and 0.5% Mo has the highest levels of absorbed power for certain temperatures, 3.0% Mo has one of the highest levels of absorbed power regardless of temperature, making it the best choice for optimal efficiency.

Chapter 7

Conclusion

7.1 Computer Model

In this Thesis, we have undertaken the first steps in the development of CAD tools for a MMW HX. The efficient FDTD EM and coupled EM-thermal models have been created for a simplified scenario representing the first physical prototype of the device. That scenario consists of a single rectangular block of an AlN:Mo composite backed by a thin metal plate and irradiated by the plane MMW at 95 GHz. Different Mo concentrations, ranging from 0.25 to 4.0%, have been considered to identify the material composition leading to the most uniform heating and maximum energy efficiency of the system. The models have been supplied with experimental data on temperature-dependent EM and thermal material parameters of those AlN:Mo composites. The output of the FDTD EM model simulating the EM field and dissipated power in a similar scenario at the microwave frequency of 2.45 GHz has been benchmarked against the output of an FEM model. Nearly identical patterns produced by both numerical techniques have confirmed sufficient adequacy of the developed models and their applicability in CAD of a MMW HX.

Thanks to the input data on the temperature-dependent material parameters, the EM-thermal coupled model is capable of accurately simulating the time evolution of volumetric temperature fields up to 1,000°C. Under the condition of full thermal insulation, the heating time step in the iterative solving of the coupled problem is dictated by the temperature step in tabulated data on the material parameters. However, under an explicit thermal boundary condition applied on the interface between the ceramic block and the metal plate, the HTS is influenced by non-uniformity of temperature distributions in the direction of wave propagation and should be chosen in accordance

with convergence of the results on temperature. Computational time may be much longer in this case, but can be reduced by compromising with higher computational error.

7.2 Operational Functionality of the Susceptor

The conducted computational study shows that when the incident plane wave carries a power equal to 100 W, the 10 mm cubic AlN:Mo blocks are heated quickly and with a very high level of uniformity. The heating rate depends on the concentration of Mo, with higher contents (ensuring higher dielectric losses) leading to faster heating; depending on the material, the temperature of the ceramic block takes as little as 60 to 95s to go from 20 to 1,000°C.

While all compositions of the AlN:Mo blocks are heated highly uniformly, the composite with 3-4% of Mo appears to be the most energy efficient: it absorbs the most (up to around 50-55%) power of the incoming plane wave. In the regime with an explicit high temperature (600, 700, 800°C) maintained in the metal plate on the back surface of the block, the temperature gradient in the materials with 3-4% of Mo reaches up to 90-100°C. These values are below the limits that would make operations of this composite less stable and reliable, so the samples of AlN:Mo with Mo concentrations of 3-4% can be recommended for use in the first physical prototype.

7.3 Future Computational Studies

The initial progress in the development of CAD tools for designing a MMW HX and advancing the technology of wireless power transfer appears to be successful, and continuation of the presented effort is highly feasible. The next steps may address the following issues:

1. The dependency of accuracy of the EM-thermal coupled simulation on the HTS in the scenario with an explicit thermal boundary condition (and thus with non-uniform temperature distributions) has never been reported before, neither for microwave, nor MMW frequency range applications, so a special computational study aiming to find out which parameters are particularly responsible for this effect is necessary. This can be done in the framework of a series of dedicated computational experiments with the model developed in this Thesis.

2. The first physical prototype of the MMW HX is planned to have 16 or 20 AlN:Mo blocks adjacent to a common metal plate. The model developed and employed in this study for a single block can be upgraded to include several (e.g., four) of them, like in Figure 1.1, without

prohibitive computational resources. In the presence of a common baseplate and small air gaps between the blocks, the structure is expected to be heated differently, and the upgraded model will reveal this difference for further investigation.

3. In practical operations, a MMW HX may work with incoming waves whose incidence is different from normal. The effect of oblique incidence of the MMW field on temperature profiles and efficiency of absorption can be studied with implementation in the model of a new function defining a particular angle of orientation of the irradiating plane wave.

4. The first step in benchmarking the developed model was made in this Thesis by comparing the results of the FDTD and FEM models only on the level of EM simulation. While the FEM model in *COMSOL Multiphysics* is not practical for direct modeling of the considered MMW scenario, it is capable of simulating EM-thermal coupling in the microwave frequency range. The next level of benchmarking may therefore include *COMSOL* computations of thermal processes in the zirconia block at 2.45 GHz. Closeness of the results from both models will provide additional confidence in quality and accuracy of the developed FDTD model.

5. In order to generate modeling results which would be directly relevant to corresponding experiments with MMW beaming, the developed model should be upgraded in terms of its thermal boundary conditions. Practical AlN:Mo samples will inevitably be in contact with some holders which may be responsible for a notable heat leakage. Appropriate (Robin) thermal boundary conditions introduced in the model along with particular (determined through a series of computational experiments) values of the heat transfer coefficient are expected to mimic the case of imperfect thermal insulation and lead to more realistic results for temperature fields in real-life applications of a MMW HX.

Appendices

Appendix A

MATLAB Procedure

The below MATLAB code can be used to produce visualizations of patterns of dissipated power from output files produced during a *QuickWave* simulation. The feMatrix function takes a *.fe3 file as input and outputs any desired calculations as well as 2D and 3D plots of dissipated power patterns. The feMatrix functions calls the GetfeMatrix function, which extracts the matrix of dissipated power values from the *.fe3 files. The user can then perform calculations on the matrix values within the feMatrix function. It also calls the PlotfeMatrix function, which produces the visualizations of the patterns of dissipated power.

```
1   function [] = feMatrix(fname)
2
3       %Get values from .fe3 file and put them into a matrix
4       amatrix = GetfeMatrix(fname);
5
6       %Do calculations with matrix values
7       colsum = sum(amatrix);
8       totala = sum(colsum)/(10^3);
9       totalb = sum(colsum)/(9.433);
10      disp([totala totalb sum(colsum)]);
11
12      %Plot matrix values
13      PlotfeMatrix(amatrix)
14
15  end
```

```
function amatrix = GetfeMatrix (fname)

fprintf ('\n FINDING MATRIX... \n');
    % Reading lines of the file that contain dimensions
    fid = fopen(fname,'r');
    for c = 1:50
        line = strtrim(fgets(fid));
        if contains(line, '_max')
            lineno = c;
            break;
        end
    end
    fclose(fid);

    [~, B] = textread (fname, '%s %f', 2,'headerlines', lineno-1, 'delimiter', '=');

    colnr = B(1,1);
    rownr = B(2,1);
    disp([rownr colnr]);

    fid = fopen(fname,'r');
    for i = 1:50
        line = strtrim(fgets(fid));
        if contains(line, 'Ydist')
            lineno = i;
            break;
        end
    end
    fclose(fid);

    startrow = lineno+3; %can find by counting lines in file
    endrow = startrow + rownr - 2; %2 rows of the matrix are borders
    startcol = 0;
    endcol = startcol + colnr;
    disp([startrow endrow startcol endcol]);

    %Reading matrix
    amatrix = dlmread (fname, ' ', [startrow startcol endrow endcol]);

    %Write matrix values to Excel file
    xlswrite('Matrix.xlsx',amatrix)
end
```

```
function [] = PlotfeMatrix (amatrix)
    %visualizing matrix in 2D
    figure
    colormap(jet);
    imagesc(amatrix(:,:,:));
    colorbar;
    title('2D Pattern of Dissipated Power');

    %Plot dissipated power peaks in 3D
    figure
    surf(amatrix);
    shading interp;
    title('Peaks of Dissipated Power');

end
```

Appendix B

*.pmo Files

Below are *.pmo files containing input data for *QuickWave* for AlN:Mo with 0.25, 0.5, 1.0, 2.0, and 4.0 % Mo concentrations. Each file's name matches the name used in *QuickWave* for the corresponding material. For example, a material is defined with the name AlN+Moly1 and its corresponding *.pmo file is named AlN+Moly1.pmo. The *.pmo files for the Dirichlet boundary condition scenario are formatted the same way as the files pictured in Figures B.1 and B.2, but they start at T_c, the temperature at which the metal plate is held constant. For T_c = 700°C, the *.pmo file starts at 700°C and ends at 1000°C.

```
# AlN:Mo 0.5% composite media file for QW-BHM module (Aug 2018 VVY)
# Measurements by AFRL-Kirtland, Albuquerque, NM
# Post-processing of measured data by IMMG/CIMS/WPI, Worcester, MA
# DATA FROM 20 C to 1000 C
```

!Temperature	Enthalpy	EPa	SIGa	SpecHeat	Density	Ka
# C	J/cm3		S/m	J/gC	g/cm^3	W/cmC
20	0	8.76	0.1916	0.704	3.33	1.2416
100	202.9	8.82	0.2127	0.819	3.33	1.0824
200	492.7	8.90	0.2391	0.921	3.33	0.9087
300	810.8	8.98	0.2655	0.989	3.33	0.7622
400	1147.8	9.06	0.2919	1.034	3.33	0.6421
500	1497.4	9.14	0.3183	1.065	3.33	0.5475
600	1855.8	9.22	0.3446	1.088	3.33	0.4774
700	2221.1	9.30	0.3710	1.106	3.33	0.4311
800	2592.2	9.38	0.3974	1.122	3.33	0.4075
900	2968.1	9.46	0.4238	1.135	3.33	0.4058
1000	3347.3	9.54	0.4502	1.142	3.33	0.4252

```
# AlN:Mo 0.25% composite media file for QW-BHM module (June 2018 VVY)
# Measurements by AFRL-Kirtland, Albuquerque, NM
# Post-processing of measured data by IMMG/CIMS/WPI, Worcester, MA
# DATA FROM 20 C to 1000 C
```

!Temperature	Enthalpy	EPa	SIGa	SpecHeat	Density	Ka
# C	J/cm3		S/m	J/gC	g/cm^3	W/cmC
20	0	8.61	0.1504	0.702	3.32	1.4028
100	202.0	8.68	0.1673	0.820	3.32	1.1275
200	491.3	8.76	0.1884	0.923	3.32	0.8719
300	809.2	8.84	0.2095	0.991	3.32	0.6989
400	1145.7	8.92	0.2306	1.036	3.32	0.5917
500	1494.5	9.00	0.2518	1.066	3.32	0.5333
600	1852.1	9.08	0.2729	1.088	3.32	0.5069
700	2216.4	9.16	0.2940	1.107	3.32	0.4957
800	2586.4	9.24	0.3151	1.123	3.32	0.4829
900	2961.4	9.32	0.3362	1.136	3.32	0.4515
1000	3339.6	9.40	0.3573	1.142	3.32	0.3848

Figure B.1: .*pmo files for the FDTD coupled EM-thermal model in *QuickWave* for 0.25 and 0.5% Mo.

```
# AlN:Mo 1.0% composite media file for QW-BHM module (Aug 2018 VVY)
# Measurements by AFRL-Kirtland, Albuquerque, NM
# Post-processing of measured data by IMMG/CIMS/WPI, Worcester, MA
# DATA FROM 20 C to 1000 C
```

!Temperature	Enthalpy	EPa	SIGa	SpecHeat	Density	Ka
# C	J/cm3		S/m	J/gC	g/cm^3	W/cmC
20	0	9.09	0.2644	0.692	3.37	1.3003
100	201.8	9.16	0.2855	0.805	3.37	1.0337
200	490.3	9.24	0.3119	0.906	3.37	0.8284
300	807.1	9.32	0.3383	0.974	3.37	0.7107
400	1142.9	9.40	0.3647	1.019	3.37	0.6360
500	1491.5	9.48	0.3911	1.050	3.37	0.5737
600	1849.2	9.56	0.4175	1.073	3.37	0.5079
700	2214.3	9.64	0.4439	1.093	3.37	0.4367
800	2585.7	9.72	0.4703	1.111	3.37	0.3729
900	2962.6	9.80	0.4966	1.126	3.37	0.3435
1000	3343.8	9.88	0.5230	1.136	3.37	0.3897

```
# AlN:Mo 2.0% composite media file for QW-BHM module (Aug 2018 VVY)
# Measurements by AFRL-Kirtland, Albuquerque, NM
# Post-processing of measured data by IMMG/CIMS/WPI, Worcester, MA
# DATA FROM 20 C to 1000 C
```

!Temperature	Enthalpy	EPa	SIGa	SpecHeat	Density	Ka
# C	J/cm3		S/m	J/gC	g/cm^3	W/cmC
20	0	9.96	0.6318	0.681	3.44	1.3754
100	202.8	10.04	0.6655	0.793	3.44	1.1184
200	492.6	10.14	0.7078	0.892	3.44	0.8962
300	811.0	10.24	0.7500	0.959	3.44	0.7505
400	1148.6	10.34	0.7922	1.004	3.44	0.6524
500	1499.1	10.44	0.8344	1.035	3.44	0.5802
600	1859.2	10.54	0.8766	1.059	3.44	0.5192
700	2226.9	10.64	0.9189	1.079	3.44	0.4623
800	2601.5	10.74	0.9611	1.099	3.44	0.4088
900	2982.4	10.84	1.0033	1.116	3.44	0.3662
1000	3368.5	10.94	1.0455	1.129	3.44	0.3486

```
# AlN:Mo composite (4% Mo) media file for QW-BHM module (Aug 2018 VVY)
# Measurements by AFRL-Kirtland, Albuquerque, NM
# Post-processing of measured data by IMMG/CIMS/WPI, Worcester, MA
# DATA FROM 20 C to 1000 C
```

!Temperature	Enthalpy	EPa	SIGa	SpecHeat	Density	Ka
# C	J/cm3		S/m	J/gC	g/cm^3	W/cmC
20	0	13.45	6.1587	0.658	3.57	1.3452
100	203.6	13.56	6.3276	0.767	3.57	1.0979
200	494.7	13.69	6.5387	0.864	3.57	0.8928
300	814.6	13.82	6.7498	0.928	3.57	0.7631
400	1153.7	13.95	6.9609	0.972	3.57	0.6750
500	1506.4	14.08	7.1720	1.004	3.57	0.6045
600	1869.6	14.21	7.3831	1.031	3.57	0.5372
700	2242.1	14.34	7.5942	1.056	3.57	0.4690
800	2623.5	14.47	7.8053	1.081	3.57	0.4052
900	3013.8	14.60	8.0165	1.105	3.57	0.3611
1000	3411.8	14.73	8.2276	1.124	3.57	0.3616

Figure B.2: .*pmo files for the FDTD coupled EM-thermal model in *QuickWave* for 1.0, 2.0, and 4.0% Mo.

Appendix C

*.pm2 Files

The *.pm2 file used to apply Dirichlet boundary conditions in *QuickWave* are shown in Figure C.1. The lower temperature value is the starting temperature of the ceramic block, while the highest is the maximum temperature defined in the *.pmo file. The values for Enthalpy, taken from a material's *.pmo file, can be defined in two different ways that produce the same results. The first way, shown in the *.pm2 file for 0.25%, takes the Enthalpy values as they are in the *.pmo files for the corresponding temperatures. The second way, shown in the *.pm2 file for 0.5%, sets the Enthalpy for the lower temperature to 0 and the Enthalpy for the higher temperature to the difference between the two Enthalpy values in the *.pmo file. The *.pm2 files are named to identify the boundary to which they apply. The below *.pm2 files define the boundary between the ceramic block and the air and are named in the format AlN-Moly1-700_air.pm2, where AlN-Moly1-700 is the name of the ceramic defined in *QuickWave*.

0.25%

```
# Boundary conditions definition file for boudary between air and ceramic
!Temperature    Enthalpy    Ha
700             2216.4      0
1000            3339.6      0
```

0.5%

```
# Boundary conditions definition file for boudary between air and ceramic
!Temperature    Enthalpy    Ha
700             0           0
1000            1126.2      0
```

1.0%

```
# Boundary conditions definition file for boudary between air and ceramic
!Temperature    Enthalpy    Ha
700             0           0
1000            1129.5      0
```

2.0%

```
# Boundary conditions definition file for boudary between air and ceramic
!Temperature    Enthalpy    Ha
700             0           0
1000            1141.6      0
```

3.0%

```
# Boundary conditions definition file for boudary between air and ceramic
!Temperature    Enthalpy    Ha
700             2222.7      0
1000            3372.0      0
```

4.0%

```
# Boundary conditions definition file for boudary between air and ceramic
!Temperature    Enthalpy    Ha
700             0           0
1000            1169.7      0
```

Figure C.1: *.pm2 files for the FDTD coupled EM-thermal model in *QuickWave* for each concentration of Mo.

Bibliography

[1] A. Datta and R. Anartheswaran, *Handbook of Microwave Technology for Food Application.* CRC Press, 2001.

[2] L. Feher, *Energy Efficient Microwave Systems: Materials Processing Technologies for Avionic, Mobility and Environmental Applications.* Springer, 2009.

[3] N. Leadbeater, *Microwave Heating as a Tool for Sustainable Chemistry.* CRC Press, 2010.

[4] M. Willert-Porada, *Advances in Microwave and Radio Frequency Processing.* Springer, 2006.

[5] S. Chandrasekaran, S. Ramanathan, and T. Basak, "Microwave material processing - a review," *AlChE J.*, vol. 58, no. 2, pp. 330–363, 2012.

[6] K. Komurasaki and K. Tabata, "Development of a novel launch system microwave rocket powered by millimeter-wave discharge," *Intern. J. of Aerospace Engineering*, vol. 2018, 9247429, 9 p.

[7] K. Parkin, L. DiDomenico, and F. Culick, "The microwave thermal thruster concept," *2nd Intern. Symp. on Beamed Energy Propulsion*, pp. 418–429, 2004.

[8] N. Komerath and A. Kar, "Retail beamed power using millimeter waves: survey," *ACM J. Emergin Technologies in Computing Systems*, vol. 8, no. 3, pp. 18:1–18:25, 2012.

[9] A. Etinger, M. Pilossof, B. Litvak, D. Hardon, M. Einat, B. Kapilevich, and Pinhasi, "Characterization of a schottky diode rectanna for millimeter wave power beaming using high power radiation sources," *Acta Physica Polonica Series*, vol. 131, no. 5, pp. 1280–1284, 2017.

[10] B. Hoff, M. Hilario, B. Jawdat, J. Mackey, A. Baros, F. Dynys, V. Yakovlev, C. Andraka, K. Armijo, E. Savrun, and I. Rittersdort, "Millimeter wave interactions with high temperature

materials and their applications to power beaming," in *Proc. 52nd IMPI Microwave Power Symp., Long Beach, CA*, June 2018, pp. 82–83.

[11] B. Jawdat, B. Hoff, M. Hilario, P. Pelletier, A. Baros, F. Dynys, and T. Sabo, "Composite ceramics for power beaming," in *Proc. 2017 IEEE Wireless Power Transfer Conference*, 2017.

[12] A. Mohekar, J. Gaone, B. Tilley, and V. Yakovlev, "A 2d coupled electromagnetic, thermal and fluid flow model: application to layered microwave heat exchangers," in *IEEE MTT-S Intern. Microwave Symp. Dig., Philadelphia, PA*, June 2018, pp. 1389–1392.

[13] ——, "Multiphysics simulation of temperature profiles in a triple-layer model of a microwave heat exchanger," in *Proc. 52nd IMPI's Microwave Power Symp., Long Beach, CA, June 2018*, 2018b, pp. 33–35.

[14] M. Celuch and W. Gwarek, "Properties of the fdtd method relevant to the analysis of microwave power problems," *J. of Microwave Power and Electromag. Energy*, vol. 41, no. 4, pp. 62–80, 2006.

[15] P. Kopyt and M. Celuch, "Coupled electromagnetic-thermodynamic simulations of microwave heating problems using the fdtd algorithm," *J. of Microwave Power and Electromag. Energy*, vol. 41, no. 4, pp. 18–29, 2007.

[16] V. Yakovlev, "Examination of contemporary electromagnetic software capable of modeling problems of microwave heating," in *Advances in Microwave and Radio Frequency Processing*, M. Willert-Porada, Ed. Springer, 2006, pp. 178–190.

[17] R. Suga, O. Hashimoto, R. K. Pokharel, K. Wada, and S. Watanabe, "Analytical study on change of temperature and absorption characteristics of a single-layer radiowave absorber under irradiation electric power," *IEEE Transactions on Electromagnetic Compatibility*, vol. 47, no. 4, pp. 866–871, 2005.

[18] J. Zhong, S. Liang, Y. Yuan, and Q. Xiong, "Coupled electromagnetic and heat transfer ode model for microwave heating with temperature-dependent permittivity," *IEEE Transactions on Microwave Theory and Techniques*, vol. 64, no. 8, pp. 2467–2477, 2016.

[19] M. Sadiku, *Numerical Techniques in Electromagnetics*, 2nd ed. CRC Press, 2000.

[20] T. Koutchma and V. Yakovlev, "Computer modeling of microwave heating processes for food preservation," in *Mathematical Analysis of Food Processing*, M. Farid, Ed. CRC Press, 2010, pp. 625–657.

[21] V. Yakovlev, "Introduction to multiphysics modeling in microwave power engineering," *Short Course, IMPI's 52nd Annual Microwave Power Symp. (IMPI 52), Long Beach, CA*, June 2018.

[22] QuickWave™, ver. 2018, QWED Sp. z o. o., 1998-2019, http://www.qwed.eu/.

[23] M. Celuch and P. Kopyt, "Modeling of microwave heating of foods," in *Development of Packaging and Products for Use in Microwave Ovens*, M. Lorence and P. Pesheck, Eds. Woodhead Publishing, 2009, pp. 305–348.

[24] V. Yakovlev, S. Allan, M. Fall, and H. Shulman, "Computational study of thermal runaway in microwave processing of zirconia," *Microwave and RF Power Applications*, pp. 303–306, 2011.

[25] A. Baros and M. Hilario, "95 GHz power beaming demonstration," HPEM CTC, AFRL, Kirtland AFB, 2018.

[26] B. Hoff, M. Hilario, S. Hayden, R. Grudt, A. Baros, F. Dynys, and M. Ostraat, "Characterization of aln-based ceramic composites for use as millimeter wave susceptor materials at high temperature: high temperature thermal properties of aln:mo with 0.25% to 4.0% mo by volume," *MRS Advances*, pp. 1–12, 2019.

[27] American Beryllia Inc., "Thermal conductivity," https://www.americanberyllia.com/beryllium-oxide.

[28] K. Ayappa, H. Davis, E. Davis, and J. Gordon, "Analysis of microwave heating of materials with temperature-dependent properties," *AIChE J.*, vol. 37, no. 3, pp. 313–322, 1991.

[29] M. Hossan and P. Dutta, "Effects of temperature dependent properties in electromagnetic heating," *Intern. J. of Heat and Mass Transfer*, vol. 55, pp. 3412–3422, 2012.

[30] K. Kashimura, H. Sugawara, M. Hayashi, T. Mitani, and N. Shinohara, "Microwave heating behavior and microwave absorption properties of barium titanate at high temperatures," *AIP Advances*, vol. 6, 065001, 2016.

[31] J. Gaone, B. Tilley, and V. Yakovlev, "Electromagnetic heating control via high-frequency resonance of a triple-layer laminate," *J. of Engng Math.*, vol. 114, no. 1, pp. 65–86, 2019.

[32] M. Hilario, B. Hoff, B. Jawdat, F. Dynys, and J. Wang, "High temperature millimeter-wave permittivity measurement setup for beamed energy heat exchangers," in *55th AIAA Aerospace Sciences Meeting*, 2017.

[33] M. Hilario, B. Hoff, B. Jawdat, A. Cohick, M. Lanagan, F. Dynys, J. Mackey, and J. Gaone, "W-band complex permittivity measurements at high temperature using freespace methods," in *IEEE Trans. Compon. Packag. Manuf. Technol.*, 2019 (accepted).

[34] P. Kumi, V. Yakovlev, M. Hilario, B. Hoff, and I. Rittersdorf, "Computational characterization of a composite ceramic layer for a millimeter wave heat exchanger," in *Proc. of the 12th Intern. Conf. on Scientific Computing in Electrical Engng, Taormina, Italy*, September 2018, 8 p.

[35] COMSOL Multiphysics^{TM}, ver. 5.3a, COMSOL AB, Stockholm, Sweden, 2018, www.comsol.com.

[36] D. Salvi, D. Boldor, J. Ortego, G. Aita, and C. Sabliov, "Numerical modeling of continuous flow microwave heating: a critical comparison of comsol and ansys," *J. of Microwave Power and Electromag. Energy*, vol. 44, no. 4, pp. 187–197, 2010.

[37] D. Salvi, D. Boldor, G. Aita, and C. Sabliov, "Comsol multiphysics model for continuous flow microwave heating of liquids," *J. of Food Engineering*, vol. 104, no. 3, pp. 422–429, 2011.

[38] P. Langer, M. Maeder, C. Guist, M. Krause, and S. Marburg, "More than size elements per wavelength: the practical use of structural finite element models and their accuracy in comparison with experimental results," *J. of Computational Acoustics*, vol. 25, no. 4, p. 23, 2017.